Modelling Atmospheric Mineral Aerosol Chemistry to Predict Heterogeneous Photooxidation of SO_2

Zechen Yu, Myoseon Jang, and Jiyeon Park
P.O. Box116450, Department of Environmental Engineering Sciences, Engineering School of Sustainable Infrastructure and Environment, University of Florida, Gainesville, FL, USA, 32611
Corresponding author: Myoseon Jang, mjang@ufl.edu

Abstract.

The photocatalytic ability of airborne mineral dust particles is known to heterogeneously promote SO_2 oxidation, but prediction of this phenomenon is not fully taken into account by current models. In this study, the Atmospheric Mineral Aerosol Reaction (AMAR) model was developed to capture the influence of air–suspended mineral dust particles on sulfate formation in various environments. In the model, SO_2 oxidation proceeds in three phases including the gas phase, the inorganic–salted aqueous phase (non–dust phase), and the dust phase. Dust chemistry is described as the absorption–desorption kinetics of SO_2 and NO_x (partitioning between the gas phase and the multilayer coated dust). The reaction of absorbed SO_2 on dust particles occurs *via* two major paths: autoxidation of SO_2 in open air and photocatalytic mechanisms under UV light. The kinetic mechanism of autoxidation was first leveraged using controlled indoor chamber data in the presence of Arizona Test Dust (ATD) particles without UV light, and then extended to photochemistry. With UV light, SO_2 photooxidation was promoted by surface oxidants (OH radicals) that are generated *via* the photocatalysis of semiconducting metal oxides (electron−hole theory) of ATD particles. This photocatalytic rate constant was derived from the integration of the combinational product of the dust absorbance spectrum and wave–dependent actinic flux for the full range of wavelengths of the light source. The predicted concentrations of sulfate and nitrate using the AMAR model agreed well with outdoor chamber data that were produced under natural sunlight. For seven consecutive hours of photooxidation of SO_2 in an outdoor chamber, dust chemistry at the low NO_x level was attributed to 55% of total sulfate (56 ppb SO_2, 290 μg m^{-3} ATD, and NO_x less than 5 ppb). At high NO_x (>50 ppb of NO_x with low hydrocarbons), sulfate formation was also greatly promoted by dust chemistry, but it was suppressed by the competition between NO_2 and SO_2 that both consume the dust–surface oxidants (OH radicals or ozone).

1 Introduction

The surface of mineral dust particles is able to act as a sink for various atmospheric trace gases such as sulfur dioxide (SO_2), nitrogen oxides (NO_x, e.g. NO and NO_2), and ozone (O_3). Among trace gases, SO_2 has received much attention because heterogeneous oxidation of SO_2 produces nonvolatile sulfuric acid, which is readily involved in the acidification of particles or the reaction with dust constituents such as alkaline metals (K^+, Na^+) or metal oxides (e.g. α–Al_2O_3 and Fe_2O_3). Such modification of the chemical composition of dust particles can influence the hygroscopic properties of mineral dust, which is essential to activate cloud condensation nucleation (Krueger et al., 2003;Zhang and Chan, 2002;Vlasenko et al., 2006;Liu et al., 2008;Tang et al., 2016).

Metal oxides (e.g. TiO_2 and Al_2O_3) have frequently been used in many laboratories to study the key role of mineral dust in the heterogeneous oxidation of SO_2 (Goodman et al., 2001;Usher et al., 2002;Zhang et al., 2006). However, these laboratory studies have been limited to a certain type of metal oxide and autoxidation of SO_2 without a light source. To date, only a few studies have attempted to study the photocatalytic characteristics of mineral dust in the oxidation of SO_2 and NO_x. For example, as noted by Park and Jang (2016), the reactive uptake coefficient ($\gamma_{SO_4^{2-}}$) of SO_2 in the presence of dry Arizona Test Dust (ATD) particles under UV light was one order of magnitude higher (1.16×10^{-6} using an indoor chamber with a light mix of UV–A and UV–B light) than that from autoxidation (1.15×10^{-7}) without a light source. Using an aerosol flow tube, Dupart et al. (2014) observed that the uptake rate of NO_2 by ATD dust particles was significantly enhanced (by four times) under UV–A irradiation compared to dark conditions. Field observations have also reported the promotion of SO_2 photooxidation in the presence of mineral dust. For instance, near Beijing, China (ground–based campaign in 2009), and in Lyon, France (remote–sensing campaign in 2010), Dupart et al. (2012) found that mineral dust was a source of OH radicals under UV radiation that promoted sulfate formation.

Semiconducting metal oxides (e.g. α–Al_2O_3, α–Fe_2O_3, and TiO_2) act as a photocatalyst in mineral dust particles that can yield electron (e^-_{cb})–hole (h^+_{vb}) pairs, and that they are involved in the production of strong oxidizers, such as superoxide radical anions (O_2^-) and OH radicals (Linsebigler et al., 1995;Hoffmann et al., 1995;Thompson and Yates, 2006;Cwiertny et al., 2008;Chen et al., 2012;Dupart et al., 2014;Colmenares and Luque, 2014). These oxidizers enable

rapid oxidation of adsorbed SO_2 and NO_x on the surface of mineral dust particles. For example, using transmission FTIR spectroscopy and X–ray photoelectron spectroscopy, Nanayakkara et al. (2012) observed the oxidation of SO_2 by the photo–catalytically generated OH radicals in the presence of titanium oxide particles. The heterogeneous formation of sulfate and nitrate can be highly variable and dependent on the chemical characteristics of dust aerosol (Gankanda et al., 2016). Authentic mineral dust particles differ from pure metal oxides in chemical composition. For example, Wagner et al. (2012) reported that the content of metal oxides in Saharan dust samples from Burkina Faso includes 14% Al_2O_3, 8.4% Fe_2O_3, and 1.2% TiO_2.

Most research on dust photochemistry has been limited to qualitative studies and lacks kinetic mechanisms that are linked to a predictive model. The typical wave–dependent photolysis of gas–phase trace gases has long been subject to atmospheric photochemistry. This photolysis rate is a first–order reaction and is calculated *via* the coupling actinic flux (the quantity of photons) with the characteristics (cross section area and quantum yield) of a light–absorbing molecule (McNaught and Wilkinson, 1997). In order to model dust photochemistry, the integration of wavelength–dependent actinic flux with the photocatalytic activity of mineral dust is needed.

In addition to sunlight intensity, humidity also influences heterogeneous dust chemistry. Humidity governs particle water content, which influences the gas–dust sorption process of trace gases (Navea et al., 2010) and the formation of dust–phase oxidants. Huang et al. (2015) found that the $\gamma_{SO_4^{2-}}$ of SO_2 autoxidation in ATD particles increased by 142% because of the relative humidity (RH) changed from 15% to 90%. In the presence of UV light, the particle water content can act as an acceptor for h^+_{vb} and produce surface OH radicals, promoting heterogeneous photochemistry of SO_2 on mineral dust. In the presence of UV light, Shang et al. (2010) reported that sulfate production on the surface of TiO_2 increased by five times because of the increase of RH from 20% to 80%. Park and Jang (2016) also reported the exponential increase in $\gamma_{SO_4^{2-}}$ as the RH increased from 20% to 80% for both autoxidation and photooxidation of SO_2 in the presence of ATD particles. A few studies have attempted to simulate sulfate formation in the presence of mineral dust at regional scales using laboratory–generated kinetic parameters (Tang et al., 2004;Li and Han, 2010;Dong et al., 2016). However, $\gamma_{SO_4^{2-}}$ applied to the regional simulations originated from pure and dry metal oxides without UV light, and thus will differ from those of ambient dust exposed to natural sunlight. It is expected that the typical regional simulations during dust events might underestimate the formation of sulfate.

In this study, the Atmospheric Mineral Aerosol Reaction (AMAR) model was developed to predict atmospheric oxidation of trace gases such as SO_2 and NO_2 under ambient conditions. The kinetic mechanisms of dust–driven photochemistry, including autoxidation and photooxidation of SO_2, was newly established in the model. The rate constant of dust photoactivation, which forms electron–hole pairs and sources dust–driven oxidants, was integrated into the model. The influence of meteorological variables, such as humidity, temperature and sunlight, on SO_2 oxidation was investigated using the resulting AMAR model. The model also addresses the kinetic mechanism to simulate how atmospheric major pollutants such as NO_x and ozone are engaged in the oxidation of SO_2 in the presence of airborne dust particles. For environmental scenarios, the model was applied for polluted urban conditions (e.g. hydrocarbon ppbC/NO_x ppb < 5) and low NO_x conditions (e.g. hydrocarbon ppbC/NO_x ppb > 5). The reaction rate constants for both autoxidation and photocatalytic reactions of SO_2 were obtained through the simulation of indoor chamber data, which were previously generated under various meteorological and environmental conditions (Park and Jang, 2016). The suitability of the resulting AMAR model was tested against sulfate formation in a large outdoor smog chamber at the University of Florida Atmospheric Photochemical Outdoor Reactor (UF–APHOR) under natural sunlight. The AMAR model of this study will vastly improve the accuracy of the prediction of sulfate and nitrate formation in regional and global scales where dust emission is influential.

2 Experimental

2.1 Chamber experiments

The indoor chamber data of this study was obtained from the recent laboratory study by Park and Jang (2016) to determine the kinetic rate constants that are needed to develop the AMAR model. The indoor chamber operation has been reported previously (Park and Jang 2016) (Also see Sect. S1). The indoor chamber data are listed in Table 1. The outdoor chamber experiments were performed in the UF–APHOR dual chambers (52 m^3 for each chamber) to test the suitability of AMAR model to ambient condition. The light irradiation of the indoor–UV light and the sunlight are shown in Fig. S1. The detailed description of the operation of outdoor chamber is also described in Sect. S1. The outdoor experimental conditions for SO_2 heterogeneous reaction in the presence of mineral dust particles are listed in Table 2.

2.2 Light absorption of ATD particles

The absorbance spectrum of ATD particles was measured to develop the reaction rate constants in the kinetic model. The detailed procedure for light absorption measurement of particle samples can be found in the previous study (Zhong and Jang, 2011). The particle size distribution of ATD is shown in Fig. S2. The suspended dust particles were sampled on a Teflon coated glass fiber filter for 20 minutes. The masses difference of dust sample was measured using a microbalance (MX5, Mettler Toledo, Columbus, OH). The light absorbance of the dust filter sample (Abs_{ATD}) was measured using a Perkin–Elmer Lambda 35 UV–visible spectrophotometer equipped with a Labsphere RSA–PE–20 diffuse–reflectance accessory. The absorbance spectrum was normalized by particle mass and calculated to obtain the mass absorbance cross section (See Sect. S1 in Supporting Information). The resulting absorbance cross section and quantum yield of ATD dust are shown in Fig. S3.

3 AMAR model description

The overall schematic of the AMAR model is shown in Fig 1. In the model, the total sulfate mass concentration ($[SO_4^{2-}]_T$, μg m^{-3}) is predicted from the reactions in three phases: the sulfate formed in the gas phase ($[SO_4^{2-}]_{gas}$, μg m^{-3}), the sulfate from the aqueous phase ($[SO_4^{2-}]_{aq}$, μg m^{-3}) and the sulfate from dust–driven chemistry ($[SO_4^{2-}]_{dust}$, μg m^{-3}). The key components of the model consist of the partitioning process and the kinetic mechanisms in three phases.

(1) The gaseous inorganic species (e.g. SO_2, NO_x and ozone) are partitioned onto both inorganic–salt (sulfuric acid and its salts) seeded aqueous particles and mineral dust particles. ATD particles are known to be coated with the multilayer of water due to their high affinity to water (Gustafsson et al., 2005) (Sect. 3.2.1). Therefore, we assumed that gas–dust partitioning of tracers on multilayer water is processed in absorption mode. (2) SO_2 oxidation in the gas phase is simulated using mechanisms previously reported in the literature (Byun and Schere, 2006;Sarwar et al., 2013;Sarwar et al., 2014;Binkowski and Roselle, 2003) (Table. S1).

(3) The partitioned SO_2 is heterogeneously oxidized in the inorganic–salt seeded aqueous phase based on the previously reported mechanisms (Liang and Jacobson, 1999).

(4) The formation of sulfate ($[SO_4^{2-}]_{dust}$) in the dust phase is approached using two kinetic sub–modules: the production of sulfate ($[SO_4^{2-}]_{auto}$, μg m^{-3}) by autoxidation in open air and sulfate

formation ($[SO_4^{2-}]_{photo}$, μg m^{-3}) by photocatalytic reactions. Overall, dust chemistry within multilayer of water is treated by the similar manner to aqueous chemistry. However, the aqueous chemistry is operated through the whole aerosol volume and the dust chemistry is processed in the water layers on the surface of dust particles.

The simulation of chamber data using the model was performed using a kinetic solver (Morpho) (Jeffries, 1998). In these mechanisms, the symbols "g", "aq", and "d" denote the chemical species in the gas phase, inorganic–salt seeded aqueous phase, and dust phase, respectively. The unit of the concentration of chemical species is molecule per cm^3 of air. The rate constants associated with various reaction mechanisms in the AMAR model were determined by simulating pre–existing indoor chamber data obtained from controlled experimental conditions (Park and Jang, 2016). For example, the rate constant for SO_2 autoxidation (k_{auto}, s^{-1}) is semiempirically determined by fitting the predicted concentration of sulfate to the experimental data D1 in Table 1. The gas–dust partitioning constant ($K_{d,\,SO_2}$, Sect. 3.2.1) of SO_2 is dependent on temperature, aerosol water content, and acidity. $K_{d,\,SO_2}$ values were semiempirically determined using data D1–D3 (three different RHs) and the literature parameters related to the effect of temperature and acidity on $K_{d,\,SO_2}$. The rate constant (k_{photo}, cm^3 $molecule^{-1}$ s^{-1}) for the sulfate formation by photocatalytic reactions is semiempirically determined using data L1–L3 (three different RHs) in Table 1. In the presence of ozone, k_{auto} and k_{photo} are determined using datasets D4 and L4, respectively. In the following sections, the components of the AMAR model are described in detail.

3.1 SO_2 oxidation in gas phase and aerosol aqueous phase

3.1.1 Gas phase oxidation

The oxidation of SO_2 in the gas phase has been extensively studied by numerous researchers (Baulch et al., 1984; Kerr, 1984; Atkinson and Lioyd, 1984; Calvert, 1984; Graedel, 1977; Atkinson et al., 1997). In this study, the oxidation of SO_2 is described using comprehensive reaction mechanisms shown in Table S1. The mechanisms can also be simplified as follows:

$$SO_2(g) + OH \rightarrow HOSO_2 \quad \text{(R1)}$$

$$HOSO_2 + O_2 \rightarrow SO_3 + HO_2 \quad \text{(R2)}$$

$$SO_3(g) + H_2O(g) + M \rightarrow H_2SO_4(aq) + M \quad \text{(R3)}$$

$$HOSO_2 + OH(g) + M \rightarrow H_2SO_4(aq) + M \quad \text{(R4)}$$

3.1.2 Gas–aerosol partitioning

SO_2 is dissolved into hygroscopic sulfuric acid (H_2SO_4), which is formed in the gas phase, *via* a partitioning process and reacts with the aqueous phase oxidants (e.g. H_2O_2 and O_3) to heterogeneously form H_2SO_4. The chemical species that were treated by the partitioning process include SO_2, NO_x, O_3, OH, HO_2, H_2O_2, HCOOH, CH_3OOH, HNO_3, CH_3O_2, HONO, CH_3COOH, and HCHO. In the model, the partitioning process is approached using the gas–particle partitioning coefficient K_{aq,SO_2} (m^3 μg^{-1}) based on aerosol mass concentration. K_{aq,SO_2} is derived from Henry's law constant of SO_2 (K_{H,SO_2}=1.2 mol L^{-1} atm^{-1} at 298K) (Chameides, 1984),

$$K_{aq,SO_2} = \frac{K_{H,SO_2} RT}{\rho_{aq}} \quad (1)$$

where R is the ideal gas constant (J K^{-1} mol^{-1}) and ρ_{aq} (g cm^{-3}) is the density of the particle, which is calculated using inorganic thermodynamic model (E–AIM II) (Clegg et al., 1998;Wexler and Clegg, 2002;Clegg and Wexler, 2011) based on humidity and inorganic composition. The partitioning process of SO_2 on inorganic aerosol (In_{aq}, m^2 m^{-3}) is expressed as,

$$SO_2(g) + In_{aq} \rightarrow SO_2(aq) + In_{aq} \qquad k_{abs,SO_2,aq} (m^3\ m^{-2}\ s^{-1}) \quad \text{(R5)}$$

$$SO_2(aq) \rightarrow SO_2(g) \qquad k_{des\_SO_2,aq} (s^{-1}) \quad \text{(R6)}$$

$k_{abs,SO_2,aq}$ (s^{-1} m^3 m^{-2}) and $k_{des,SO_2,aq}$ (s^{-1}) are the uptake rate constant and the desorption rate constant, respectively, and are calculated as follows,

$$k_{abs,SO_2,aq} = f_{abs,aq} \frac{\omega_{SO_2} f_{aq,M2S}}{4} \quad (2)$$

$$k_{des,SO_2,aq} = \frac{k_{abs,SO_2,aq}}{K_{aq}} \quad (3)$$

where $f_{aq,M2S}$ (5×10^{-4}) is the coefficient to convert the aerosol mass concentration (μg m^{-3}) to the surface area concentration (m^2 m^{-3}) for particle size near 100 nm and $f_{abs,aq}$ is the coefficient for uptake process. ω_{SO_2} is the mean molecular velocity (m s^{-1}) of SO_2 and can be calculated as follows,

$$\omega_{SO_2} = \sqrt{\frac{8RT}{\pi MW}} \quad (4)$$

where MW is molecular weight (kg mol^{-1}). In our model, $f_{abs,aq}$ was set at 2×10^4 in Eq. (2) to have fast partitioning process. Table S2 summarizes the characteristic time that is estimated for

diffusion, partitioning, and the reactions of major species with OH radicals in gas, aqueous, and dust phases. In general, the characteristic time (s) of a partitioning process (order of 10^{-7} s) is much faster than gas phase oxidation (order of 10^{6} s), aqueous phase oxidation (order of 10^{3}–10^{4} s), and dust phase oxidation (order of 10^{2}–10^{3} s at presence of 200 μg m^{-3} of dust particles). The mass concentration (μg m^{-3}) of inorganic seeded aqueous phase above the efflorescent relative humidity (ERH) is also dynamically calculated for the SO_4^{2-}–NH_4^+–H_2O system. Colberg et al. (2003) semiempirically predicted ERH by fitting to the experimental data based on the ammonia–to–sulfate ratio in the SO_4^{2-}–NH_4^+–H_2O system. AMAR model utilizes these parameterizations to predict ERH dynamically. Ammonia is inevitable in our chamber study and mainly acts as a carryover from previous chamber experiments. Thus, H_2SO_4 is fully or partially neutralized by ammonia.

3.1.3 Aerosol aqueous phase reaction

The AMAR model implements the aqueous–phase chemistry that occurs in inorganic salted aqueous aerosol (SO_4^{2-}–NH_4^+–H_2O system without dust) to form $SO_4^{2-}(aq)$ and $NO_3^-(aq)$. We employed the preexisting aqueous–phase kinetic reactions involving SO_2 (Liang and Jacobson, 1999) and NO_x chemistry (Liang and Jacobson, 1999;Hoyle et al., 2016). Thus, our simulation inherits all the possible uncertainties embedded in the original kinetic data.

The SO_2 dissolved in the aqueous phase is hydrolyzed into H_2SO_3 and dissociates to form ionic species (HSO_3^- and SO_3^{2-}). SO_4^{2-}(aq) is formed by reactions of the sulfur species in oxidation state IV ($S(IV)(aq)$) with OH(aq), H_2O_2(aq), or O_3(aq) (Table S1). The dissolved HONO can also dissociate to form $NO_2^-(aq)$ and result to $NO_3^-(aq)$. Each chemical species in $S(IV)(aq)$ has a different reactivity for oxidation reactions. The distribution of chemical species is affected by aerosol acidity, which is controlled by humidity and inorganic composition. Hence, the formation of sulfate is very sensitive to aerosol acidity. For example, most of the S(IV) is consumed by H_2O_2 at pH<4, whereas most of it is consumed by O_3 at pH>4. Some strong inorganic acids, such as sulfuric acid, influence aerosol acidity. In AMAR, aerosol acidity ($[H^+]$, mol L^{-1}) is estimated at each time step by E–AIM II (Clegg et al., 1998;Wexler and Clegg, 2002;Clegg and Wexler, 2011) corrected for the ammonia rich condition (Li et al., 2015;Beardsley and Jang, 2016;Li and Jang, 2012) as a function of inorganic composition measured by a Particle Into–Liquid Sampler coupled with Ion Chromatography (PILS–IC). When the ammonia–to–sulfate ratio is greater than 0.8, the

prediction of $[H^+]$ is corrected based on the method of Li and Jang (2012). At high NO_x levels, $NO_2^-(aq)$ competes with $S(IV)(aq)$ for the reaction with OH(aq), O_3, or H_2O_2 (Table S1)(Ma et al., 2008). However, the HONO concentration becomes high at high NO_x levels and enhances SO_2 oxidation in the inorganic–salt seeded aqueous phase due to the formation of OH radicals *via* photolysis of HONO.

3.2 Heterogeneous oxidation in the presence of mineral dust particles

The heterogeneous chemistry in the presence of dust particles has been newly established in the AMAR model. The dust phase module consists of a partitioning process (Sect. 3.2.1) and heterogeneous chemistry for SO_2 and other trace gases (ozone, HONO, and NO_2) (Table 3) (Fig. 1). The heterogeneous chemistry of SO_2 is handled by autoxidation (Sect. 3.2.2) and photooxidation under UV light (Sect. 3.2.4). In dust–phase photochemistry, the central mechanism for SO_2 oxidation is operated by the surface oxidants (e.g. OH(d)), which is generated *via* the photoactivation process of semiconductive metal oxides in dust particles (Sect. 3.2.3).

3.2.1 Gas–dust particle partitioning

In an adsorptive mode, water molecules suppress partitioning of SO_2 because they compete for adsorptive sites with tracers (Cwiertny et al., 2008). However, the formation of the sulfate associated with ATD increased as increasing RH as shown in Table 1, suggesting that gas–dust partitioning is more likely operated by absorption on the multilayer coated dust with water molecules. ATD contains hygroscopic inorganic salts that form the thin water film on the surface of ATD particles when the salts are deliquescent (or above ERH). Some salts such as sulfate of magnesium and calcium can be hydrated even at low humidity (Beardsley et al., 2013;Jang et al., 2010). Gustafsson et al. (2005) reported that ATD particles showed a substantially high affinity to water compared to pure $CaCO_3$ particles. In their study, the water content of ATD particles, which is measured using the thermogravimetric method, ranges from two monolayers to four monolayers based on the BET surface area between 20%–80% relative humidity. This water layer influences the gas–dust partitioning of atmospheric tracers such as SO_2 and NO_2. The gas–dust partitioning constant ($K_{d,\,SO_2}$, $m^3\ m^{-2}$) of SO_2 is defined as,

$$K_{d,\,SO_2} = \frac{[SO_2]_d}{[SO_2]_g A_{Dust}}\ (m^3\ m^{-2}) \quad (5)$$

A_{dust} (m^2 m^{-3}) is the geometric surface concentration of ATD dust particles and is calculated by multiplying the dust mass concentration (μg m^3) by a geometric surface–mass ratio ($f_{dust,Mass\_to\_Surface}$) of ATD particles (3.066×10^{-6}, m^2 μg^{-1}). The SO_2 absorption and desorption processes for the dust phase are expressed as

$$SO_2(g) + A_{Dust} \rightarrow SO_2(d) + A_{Dust} \quad k_{abs\_SO_2,dust}(m^3\ m^{-2}\ s^{-1}) \quad (R7)$$

$$SO_2(d) \rightarrow SO_2(g) \quad k_{des\_SO_2,dust}(s^{-1}) \quad (R8)$$

$k_{abs\_SO_2,dust}$ (m^3 m^{-2} s^{-1}) and $k_{des\_SO_2,dust}$ (s^{-1}) are the absorption rate constant and the desorption rate constant, respectively. At equilibrium, the absorption rate (R7) equals the desorption rate (R8). Thus, $K_{d,\,SO_2}$ can be expressed as

$$K_{d,SO_2} = \frac{k_{abs\_SO_2,dust}}{k_{des\_SO_2,dust}}\ (m^3\ m^{-2}) \quad (6)$$

The $K_{d,\,SO_2}$ value at 20% RH is set at 1.63 (m^3 m^{-2}) based on the literature data (dust particles at 20% RH) (Adams et al., 2005;Huang et al., 2015). The characteristic time to reach to equilibrium is very short (Sect. 3.1.1). In kinetic mechanisms, $k_{ads\_SO_2,dust}$ was set at 1.7×10^3 s^{-1} m^3 m^{-2} for dry particles (20% RH) using the same approach as Eq. (2). The resulting characteristic time for $k_{ads\_SO_2,dust}$ is 10^{-6} s. The characteristic time of the reaction of SO_2 with an OH radical (10^6 molecules cm^{-3}) is about 10^6–10^7 s in gas phase and 10^5–10^6 s in both aqueous phase and dust phase.

To consider the effect of temperature on K_{d,SO_2}, the temperature dependency of $k_{des\_SO_2,dust}$ (Eq. (6)) is derived from the Henry's constant (Chameides, 1984). $K_{d,\,SO_2}$ (Eq. (5)) is also influenced by aerosol water content (Zuend et al., 2011) as well as the dissociation of H_2SO_3, which is operated by aerosol acidity ($[H^+]$) and an acid dissociation constant (Ka_{SO_2})(Martell and Smith, 1976). Thus, $k_{des\_SO_2,dust}$ is expressed as,

$$k_{des\_SO_2,dust} = 1\times10^9 \exp\left(-\frac{3100}{T}\right)/(F_{water}(1+\frac{Ka_{SO_2}}{[H^+]}))\ (s^{-1}) \quad (7)$$

Ka_{SO_2} is 0.013 (mol L^{-1}) at 298K (Martell and Smith, 1976). The influence of the dissociation of inorganic acid on $K_{d,\,SO_2}$ is accounted for by the term $(1+\frac{Ka_{SO_2}}{[H^+]})$ in Eq. (7). The estimation of $[H^+]$ is treated in the same ways as aqueous chemistry (Sect. 3.1.3).

In order to estimate K_{d,SO_2} at different RH, F_{water} (coefficient of the mass fraction of water to dust particles) was introduced into the model. The hygroscopic property of mineral dust

dynamically changes because dust can be substantially modified by direct reaction of some of its components (e.g. $CaCO_3$) with inorganic acids such as H_2SO_4 and HNO_3. When dust forms $Ca(NO_3)_2$, dust becomes more hygroscopic. Nitrate salts deliquesce at very low RH (17%) (Krueger et al., 2003; Krueger et al., 2004; William et al., 2005). $CaSO_4$ is, however, relatively hydrophobic. Nitrate salts exist only when sulfate concentrations is very low. In the model, F_{water} is associated with the hygroscopic property of indigenous dust (first term in Eq. (8)), the inorganic nitrates formed from the reaction of absorbed HNO_3 with dust (second term), and the inorganic sulfate (SO_4^{2-}–NH_4^+–H_2O system, third term).

$$F_{water} = \exp(4.4\mathrm{RH}) + 3.7 f_{dust,Mass\_to\_Surface} \exp(4.4\mathrm{RH}) \frac{[\mathrm{NO_3^-}(d\_salt)]}{\mathrm{A}_{Dust}} + \frac{M_{\mathrm{in,water}}}{\mathrm{A}_{Dust}[\mathrm{Dust}]} \quad (8)$$

$M_{in,water}$ is the water concentration (μg m^{-3}) associated with inorganic sulfate and calculated using E–AIM II. Both $[\mathrm{NO_3^-}(d\_salt)]$ and $M_{in,water}$ are normalized by the mass concentration of ATD particles ([Dust], μg cm^{-3}). F_{water} is first determined using chamber simulation of SO_2 heterogeneous oxidation (first and third terms in Eq. (8)) (D1–D3 in Table 1) under varied RH levels and extended to SO_2 oxidation in the presence of NO_x (Exp. 14 April 2017 in Table 2). Among temperature, RH and aerosol acidity, the most influential variable is RH due to the variation of F_{water} (see sensitivity analysis in Sect. 5).

3.2.2 Autoxidation of SO_2 on dust surface

Typically, autoxidation of SO_2 is an oxidation process *via* the reaction of absorbed SO_2 (R7 and R8) with an oxygen molecule. In the model, $[SO_4^{2-}]_{auto}$ is defined as the sulfate resulted from any oxidation reactions (autoxidation in open air and oxidation with ozone) of SO_2 without UV light (Fig. 1). In autoxidation, the reaction of SO_2(d) with the oxygen molecules is treated as the first order reaction (assuming the concentration of oxygen is constant as 2×10^5 ppm).

$$\mathrm{SO_2(d)} \xrightarrow{\mathrm{O_2(g)}} \mathrm{SO_4^{2-}(d)} \qquad k_{auto} = 5\times10^{-6}\ (\mathrm{s^{-1}}) \quad \text{(R9)}$$

In the dark condition, the formation of sulfate is mainly sourced from autoxidation of SO_2. For comparison with other studies, we estimate the reactive uptake coefficient ($\gamma_{SO_4^{2-},auto}$) of SO_2 onto ATD dust in the absence of ozone and NO_x (Fig. 2).

$$\gamma_{SO_4^{2-},auto} = \frac{4K_{d,SO_2}k_{auto}}{\omega_{SO_2}} \quad (9)$$

$\gamma_{SO_4^{2-},auto}$ is proportional to K_{d,SO_2}, and influenced by humidity (Eq. (7)).

3.2.3 Photoactivation of dust particles and heterogeneous formation of OH radicals

The reactive uptake of SO_2 on particles is traditionally treated as a first order process (Ullerstam et al., 2003; Li et al., 2007). Such an approach is appropriate for simple autoxidation mechanisms, but not for the complex heterogeneous photooxidation of SO_2. In the AMAR model, the heterogeneous photooxidation of SO_2 is approached in three steps: (1) the formation of an e^-_{cb}–h^+_{vb} pair *via* photoactivation of dust particles, (2) the formation of OH(d) *via* the reaction of an e^-_{cb}–h^+_{vb} pair with a water or oxygen molecule, and (3) the reaction of absorbed SO_2 with the resulting OH(d) (second–order reactions) (Table S1).

The photoactivation of dust particles and the recombination reaction of an electron–hole pair (e_h) are added into the model.

$$\text{Dust} \xrightarrow{h\upsilon} \text{Dust} + \text{e\_h} \qquad k^j_{e\_h} = j_{[ATD]} \tag{R10}$$

$$\text{e\_h} \rightarrow \text{energy} \qquad k_{recom} = 1\times10^{-2}\ (\text{s}^{-1}) \tag{R11}$$

where $k^j_{e\_h}$ is the photoactivation rate constant to form e^-_{cb}–h^+_{vb} pairs and k_{recom} is the reaction rate constant of recombination (heat radiation) of an electron and a hole. The value of k_{recom} is set at a large number to prevent the accumulation of electron–hole pairs. The formation of OH(d) is expressed as

$$\text{e\_h} + O_2(\text{g}) \rightarrow \text{OH(d)} \qquad k_{OH,O_2} = 1\times10^{-22}\exp(2.3RH)\ (\text{cm}^3\ \text{molecules}^{-1}\ \text{s}^{-1}) \tag{R12}$$

k_{OH,O_2} is the reaction rate constant to form OH(d) and is first estimated using indoor chamber data (L1–L3 in Table 1) at RH 20%, 55% and 80% and then regressed against RH. The study by Thiebaud et al. (2010) reported the recombination of OH(d) near to TiO_2 surfaces. In our model, the mechanistic role of the catalytic formation of the electron–hole pairs (R10) and their recombination (R11) compensates the formation and the self–reaction of OH radicals.

In R10, $k^j_{e\_h}$ is the operational rate constant for the photoactivation of dust particles and is dependent on the photolysis rate constant, $j_{[ATD]}$ (s^{-1}). Like the typical photolysis of a gaseous molecule, the photocatalytic production of e^-_{cb}–h^+_{vb} pairs is linear to both the actinic flux ($I(\lambda)$, photons cm^{-2} nm^{-1} s^{-1}) originating from the light source and the photocatalytic property of dust particles. The value of $j_{[ATD]}$ is determined by $I(\lambda)$, the absorption cross section ($\sigma(\lambda)$, cm^2 μg^{-1}), and the quantum yield ($\phi(\lambda)$) of dust conducting matter at each wavelength range (λ, nm),

$$j_{[ATD]} = \int_{\lambda1}^{\lambda2} I(\lambda)\sigma(\lambda)\phi(\lambda)d\lambda \tag{10}$$

In the model, $\sigma(\lambda)$ is the light absorption needed to activate dust–phase semiconducting metal oxides (excitation from a ground energy level to a conducting band), and $\phi(\lambda)$ is the probability of yielding the e^-_{cb}–h^+_{vb} pair in the dust phase. Both $\sigma(\lambda)$ and $\phi(\lambda)$ cannot be directly measured because of complexity in the quantity of photoactive conducting matter in dust particles and the irradiation processes of the e^-_{cb}–h^+_{vb} pair. In order to deal with $\sigma(\lambda)\times\phi(\lambda)$, we calculated the mass absorption cross section of dust particles (MAC_{ATD}, $m^2\ g^{-1}$), which was determined using the absorption coefficient of ATD particles (b_{ATD}, m^{-1}) with the particle concentration (m_{ATD}, $g\ m^{-3}$):

$$MAC_{ATD} = \frac{b_{ATD}}{m_{ATD}} \quad (11)$$

In Eq. (11), b_{ATD} can be calculated from the absorbance of dust filter sample (Abs_{ATD}, dimensionless) measured using a reflective UV–visible spectrometer (Fig. S3):

$$b_{ATD} = \frac{Abs_{ATD}\,A}{f\,V}\ln(10) \quad (12)$$

where $A = 7.85 \times 10^{-5}$ (m^2) is the sampled area on the filter and V (m^3) is the total air volume passing through the filter during sampling. In order to eliminate the absorbance caused by filter material scattering, a correction factor (f = 1.4845) is obtained from a previous study (Zhong and Jang, 2011) and coupled into Eq. (12). The preliminary study showed that the effect of aerosol scattering on the b_{abs} values of the aerosol collected on the filter was negligible. Further, Bond (2001) reported that particle light scattering does not significantly influence spectral absorption selectivity. The MAC_{ATD} of dust particles originates from photocatalytic conducting matter (e.g. TiO_2) as well as light–absorbing matter (e.g. gypsum and metal sulfate). Thus, the MAC_{ATD} spectrum is adjusted using the known TiO_2 absorption spectrum (Reyes-Coronado et al., 2008) and applied to $\sigma(\lambda) \times \phi(\lambda)$ (Fig. S3). The resulting $\sigma(\lambda) \times \phi(\lambda)$ spectrum is applied to Eq. (10) to calculate $j_{[ATD]}$ (R10).

3.2.4 Heterogeneous photooxidation of SO_2

SO_2 is oxidized by OH(d) on the surface of ATD particles as follows,

$$SO_2(d) + OH(d) \rightarrow SO_4^{2-}(d) \qquad k_{photo} = 1.0\times10^{-12}\ (cm^3\ molecule^{-1}\ s^{-1}) \quad (R13)$$

where k_{photo} is the reaction rate constant of SO_2 with OH(d) and is estimated from gas phase reaction (R1). Combining Eq. (4), Eq. (5), R11 and R15, the reactive uptake coefficient ($\gamma_{SO_4^{2-},photo}$) of SO_2 on ATD particles under UV light can be written as,

$$\gamma_{SO_4^{2-},photo} = \frac{4K_{d,SO2}(k_{photo}[\mathrm{OH(d)}]+k_{auto})}{\omega_{SO_2}} \quad (13)$$

$\gamma_{SO_4^{2-},photo}$ is the constant at a given concentration of OH(d) (for a given light source, dust concentration, and humidity) (R10 and R12). Figure 2 illustrates $\gamma_{SO_4^{2-},photo}$ values at three different RHs, which were obtained using indoor chamber data. $\gamma_{SO_4^{2-},photo}$ is significantly influenced by both UV light and humidity. For example, $\gamma_{SO_4^{2-},photo}$ is one order of magnitude higher than $\gamma_{SO_4^{2-},auto}$ at low NO_x levels (<5 ppb), and $\gamma_{SO_4^{2-},photo}$ increased from 2.0×10^{-5} to 1.24×10^{-4} when the RH changed from 20% to 80%.

3.3 Impact of ozone and NO_x on heterogeneous chemistry of SO_2

To date, most studies of the effect of NO_x on sulfate formation have been limited to the reaction in dark condition. For example, previous laboratory studies using pure metal oxides reported the acceleration of the heterogeneous oxidation of SO_2 by NO_x in dark conditions (Ma et al., 2008;Liu et al., 2012). For the effect of ozone, the recent chamber study by Park and Jang (2016) showed significant enhancement of heterogeneous photooxidation of SO_2. In the AMAR model, the formation of sulfate is also modulated by the involvement of ozone and NO_x in both autoxidation and photochemistry on the surface of dust particles (Fig. 1).

3.3.1 Dust–phase ozone chemistry

The gas–dust partitioning coefficient of ozone is scaled using K_{d,SO_2} and the ratio of the Henry's law constant of SO_2 (K_{H,SO_2}, Eq. (1)) to that of ozone (K_{H,O_3}= 1.2×10^{-2} mol L^{-1} atm^{-1} at 298K) (Chameides, 1984),

$$K_{d,\,O_3} = K_{d,\,SO_2}\frac{K_{H,O_3}}{K_{H,SO_2}} = 7.7\times10^{-7}F_{water}\exp(\frac{2700}{T})\ (\mathrm{m^3\ m^{-2}}) \quad (14)$$

The partitioning process is also treated by the absorption–desorption kinetic mechanism as shown in R7 and R8 (Table 3: partitioning). Ozone can decay catalytically in the dust phase, forming an oxygen molecule and surface–bound atomic oxygen (Usher et al., 2003;Chang et al., 2005). The formed atomic oxygen reacts with SO_2(d) to form sulfate (Ullerstam et al., 2002;Usher et al., 2002):

$$SO_2(\mathrm{d}) + O_3(\mathrm{d}) \rightarrow SO_4^{2-}(\mathrm{d}) + O_2 \quad k_{auto,O_3}=2\times10^{-11}\ (\mathrm{cm^3\ molecules^{-1}\ s^{-1}}) \quad (R14)$$

In the presence of 300 μg m^3 of ATD particles and 60 ppb of ozone, the concentration of O_3(d) is estimated as 2.4×10^7 molecule cm^{-3}. Under this condition, the characteristic time of the

autoxidation by ozone (R14) is 2×10^3 s and is much faster than the autoxidation by oxygen (R9, 2×10^5 s). At nighttime, in the presence of ozone, the autoxidation of SO_2(d) yields a significant amount of sulfate.

Under UV light, ozone is also involved in the production of the surface oxidants (O_3^-, HO_3 radicals, and OH radicals) that further promote heterogeneous oxidation of SO_2. O_3(d) acts as an acceptor for e^-_{cb}–h^+_{vb} and forms OH(d):

$$e\_h + O_3(d) \rightarrow \cdot OH(d) + O_2 \quad k_{OH,O_3}=1\times10^{-12} \text{ (cm}^3 \text{ molecules}^{-1} \text{ s}^{-1}\text{)} \quad \text{(R15)}$$

3.3.2 Dust–phase NO_x chemistry

The gas–dust partitioning coefficient of NO_2 ($K_{d,\,NO_2}$) is treated as the same approach with ozone, using K_{d,SO_2} and the ratio of K_{H,SO_2} (Eq. (1)) to the Henry's law constant of NO_2 (K_{H,NO_2}= 1.2×10^{-2} mol L^{-1} atm^{-1} at 298K) (Chameides, 1984):

$$K_{d,\,NO_2} = K_{d,\,SO_2} \frac{K_{H,NO_2}}{K_{H,SO_2}} = 1.5\times10^{-6} F_{water} \exp\left(\frac{2500}{T}\right) \text{ (m}^3 \text{ m}^{-2}\text{)} \quad (15)$$

The absorbed NO_2 first reacts with e^-_{cb}(d) or $\cdot O_2^-$(d) on the dust surface (R10) and forms HONO(d) (Ma et al., 2008;Liu et al., 2012;Saliba and Chamseddine, 2012;Saliba et al., 2014). In AMAR, the formation of HONO(d) is simplified into:

$$e\_h + NO_2(d) \rightarrow HONO(d) \quad k_{e\_h,NO_2} = 6\times10^{-12} \text{ (cm}^3 \text{ molecules}^{-1} \text{ s}^{-1}\text{)} \quad \text{(R16)}$$

HONO(d) is further decomposed through photolysis and yields OH(d):

$$HONO(d) \xrightarrow{h\nu} \cdot OH(d) + NO \quad k^j_{HONO} = j_{[HONO]} \text{ (s}^{-1}\text{)} \quad \text{(R17)}$$

The photolysis rate constant of HONO(d) is treated with the one for gaseous HONO ($j_{[HONO]}$). Similar to autoxidation of SO_2 (Sect. 3.2.2), NO_2(d) autoxidizes to form nitrate:

$$NO_2(d) \xrightarrow{O_2(g)} NO_3^-(d) \qquad k_{auto,NO_2} = 6\times10^{-5} \text{ (s}^{-1}\text{)} \quad \text{(R18)}$$

NO_2 reacts with OH(d):

$$NO_2(d) + OH(d) \rightarrow NO_3^-(d) \quad k_{photo,NO_2} = 1\times10^{-10} \text{ (cm}^3 \text{ molecules}^{-1} \text{ s}^{-1}\text{)} \quad \text{(R19)}$$

k_{auto,NO_2} and k_{photo,NO_2} was determined using the simulation of outdoor chamber data (Exp. 14 April 2017 in Table 2). The estimation of the gas–dust partitioning coefficients of HONO ($K_{d,HONO}$) (Becker et al., 1996) and HNO_3 ($K_{d,\,HNO_3}$) (Schwartz and White, 1981) was approached using the similar method for SO_2 (Table 3). N_2O_5 forms nitrate *via* a reactive uptake process as shown in Table 3 (reaction 11).

4 Simulation of AMAR model under ambient sunlight

At the beginning of the development of the AMAR model, the kinetic parameters to predict the formation of sulfate and nitrate in the presence of ATD particles were leveraged using an indoor chamber. In order to test the feasibility of the resulting AMAR model, the UF–APHOR data using natural sunlight were simulated (Table 2). The chamber dilution (measured by CCl_4) and the wall process of gaseous compounds (e.g. ozone, SO_2, HONO, NO_2) and particles were integrated with the kinetic mechanisms to simulate UF–APHOR data (Sect. S1). As shown in Fig. 1, the model inputs are the concentration of chemical species, the amount of dust, and the meteorological variables that are commonly found at regional scales. The dual chambers allow for two controlled experiments to be performed simultaneously under the same meteorological conditions.

4.1 Simulations for different dust loadings

Figure 3 shows that the predicted $[SO_4^{2-}]_T$ is in good agreement with experimental observations, which were performed under low NO_x conditions (NO_x < 5 ppb) for two different dust loadings as well as two different SO_2 levels. The greater increase in $[SO_4^{2-}]_T$ appeared with the higher sunlight intensity (between 11 AM and 2 PM). In Fig. 3(a), the predicted $[SO_4^{2-}]_T$ increased by 63% (at 3 PM) with 290 μg m^{-3} of ATD particles compared to the $[SO_4^{2-}]_T$ without dust particles. Figure 3(b) confirms that the larger dust particle loading yields more $[SO_4^{2-}]_T$. In Fig. 3(c), $[SO_4^{2-}]_T$ was predicted with high and low initial concentrations of SO_2 for a given dust loading. The time profiles of the simulation of concentrations of NO_x, ozone, SO_2, and dust are shown in Fig. S4.

Because of the large size of dust particles, the wall processes (e.g. settling and wall deposition) of dust particles is greater than that of the sulfate particles originated from $[SO_4^{2-}]_{aq}$ (no dust). Hence, the fraction of $[SO_4^{2-}]_{dust}$ to $[SO_4^{2-}]_T$ declines over the course of the chamber experiment. To estimate how the predicted $[SO_4^{2-}]_T$ is attributed to $[SO_4^{2-}]_{aq}$+$[SO_4^{2-}]_{gas}$ (non–dust sulfate) and $[SO_4^{2-}]_{dust}$ without wall processes, Fig. 3(d), 3(e), and 3(f) are reconstructed from Fig. 3(a), 3(b), and 3(c), respectively. As shown in the inner pie chart of Fig. 3(d), a significant fraction of $[SO_4^{2-}]_T$ is attributed to dust phase chemistry ($[SO_4^{2-}]_{auto}$ + $[SO_4^{2-}]_{photo}$: 0.58). In Fig. 3(e), the fraction of final $[SO_4^{2-}]_{photo}$ to $[SO_4^{2-}]_T$ increases from 0.28 to 0.72 with the increase of dust loading from 90 μg m^{-3} to 403 μg m^{-3}. The increased dust loading promotes both the absorption of SO_2 onto dust particles and the production of dust–phase oxidants, and thus yields more sulfate

production. With the increase of the initial concentration of SO_2 from 119 ppb to 272 ppb in Fig. 3(f), the fraction of $[SO_4^{2-}]_{photo}$ and $[SO_4^{2-}]_{gas}+[SO_4^{2-}]_{aq}$ are not much changed, while $[SO_4^{2-}]_T$ increases from 16.6 μg m^{-3} to 30.1 μg m^{-3}. The elevation of the concentration of SO_2 produces more sulfate in all three phases (gas, aqueous, and dust phases). The sulfuric acid formed in the aqueous phase is hydrophilic and creates a positive feedback loop which aggravates the growth of aqueous aerosol. Overall, the variation in dust concentration is more influential on $[SO_4^{2-}]_{photo}$ than that of SO_2.

4.2 Simulation of NO_x effect

Figure 4 shows that the model performs well in predicting $[SO_4^{2-}]_T$ in various levels of NO_x. Figure 4(d) is reconstructed from Fig. 4(a), 4(b) and 4(c) to illustrate how $[SO_4^{2-}]_T$ is attributed to the aqueous–phase reaction ($[SO_4^{2-}]_{gas}+[SO_4^{2-}]_{aq}$), dust–phase autoxidation ($[SO_4^{2-}]_{auto}$), and dust photochemistry ($[SO_4^{2-}]_{photo}$). Comparing Fig. 4(b) with 4(c), $[SO_4^{2-}]_{photo}$ is suppressed at high NO_x levels because NO_2 competes for the consumption of dust–phase OH radicals with SO_2. The reduction of $[SO_4^{2-}]_T$ in the afternoon is due to the particle loss at the low concentrations of SO_2. The simulated concentrations of NO_x, ozone, SO_2, and dust are shown in Fig. S5.

The time profiles of the predicted $[NO_3^-]_T$ are also shown in Fig. 4(a), 4(b), and 4(c). In the morning, NO_2 quickly oxidizes to accumulate nitric acid in the dust phase. The dust–phase nitric acid might rapidly react with alkaline carbonates (e.g. K, Na, Ca and Mg ions) in the dust phase and form nitrate salts (NO_3^-(d_salt) in reaction 23 of dust phase reactions in Table S1). As described in Sect. 3.2.1, these nitrate salts are very hygroscopic and further enhance gas–dust partitioning of gaseous species including HNO_3, SO_2, and HONO at high humidity (in the morning). With increasing sunlight intensity, the temperature increases but humidity decreases (20%, Fig. S6) and thus increase the desorption of HNO_3. In addition to meteorological conditions, the formation of low–volatility sulfuric acid can deplete nitrate *via* evaporation of volatile nitric acid (SO_4^{2-}(d_salt) in reaction 24 and 25 of dust phase reactions in Table S1) from the dust surface. The capacity of ATD particles to form nitrate salts (or sulfate salts) is limited by the amount of carbonates and metal oxides on the surface of dust particles. This capacity is estimated to be 0.6 ppb (the number concentration of reactive sites in air), which was determined by comparing the actual aerosol acidity, as measured by the colorimetry integrated with a reflectance UV–visible

spectrometer (C–RUV), to the aerosol acidity predicted by the inorganic thermodynamic model (E–AIM II) using the inorganic composition from PILS–IC (Li et al., 2015;Beardsley and Jang, 2016). As shown in Fig. 4, the effect of HNO_3 on the heterogeneous reaction is negligible during the daytime because sulfuric acid, a strong acid, depletes partitioning of HNO_3 (Eq. (15)). At the end of the photooxidation, nitrate is slightly underestimated because some observed nitrate may be trapped under the layer of hydrophobic alkaline sulfate formed *via* aging of ATD particles (effloresced). The surface HONO(d), which formed *via* the photocatalytic process of NO_2 (R16), can influence the production of OH(d). However, the model analysis originated from the integrated reaction rate (IRR), an accumulated flux of chemical formation, suggests that the contribution of HONO(d) to OH(d) production is relatively small compared to the direct photocatalytic process caused by dust particles shown in Sect. 3.2.3.

5 Sensitivity and uncertainties

The sensitivity of sulfate prediction to major variables (e.g. temperature, humidity, sunlight profile, the concentration of SO_2 and NO_x, and dust loading) is illustrated in Fig. 5. To avoid the suppression of dust chemistry at high NO_x levels, the most sensitivity tests were performed at low levels of NO_x. The stacked chart normalized with $[SO_4^{2-}]$ in Fig. 5 shows how $[SO_4^{2-}]_T$ is attributed to $[SO_4^{2-}]_{auto}$, $[SO_4^{2-}]_{photo}$ and $[SO_4^{2-}]_{aq}+[SO_4^{2-}]_{gas}$ (non–dust chemistry).

Figure 5(a) illustrates that the reduction of $[SO_4^{2-}]_T$ at a higher temperature (273K vs. 298K) is ascribed to the decrease in the partitioning process. Figure 5(b) shows that $[SO_4^{2-}]_T$ increases by a factor of 2.8 with RH increasing from 25% to 80%. Humidity plays an important role in the modulation of both aerosol acidity and liquid water content, and ultimately influences the partitioning process (e.g. SO_2 partitioning on dust surface) and dust–phase chemistry (e.g. production of OH(d)). In the stacked column chart of Fig. 5(b), the contribution of $[SO_4^{2-}]_{dust}$ to $[SO_4^{2-}]_T$ increases from 0.73 to 0.86 with increasing RH suggesting that dust chemistry is more sensitive to humidity than aqueous phase chemistry. Figure 5(c) presents $[SO_4^{2-}]_T$ at two different sunlight intensities (winter on 12 November, 2015 vs. summer on 25 April, 2017) in Gainesville, Florida (latitude/longitude: 29.64185°/-82.347883°). As shown in Fig. 5(d), with SO_2 concentrations increasing from 20 ppb to 100 ppb, $[SO_4^{2-}]_T$ increases by a factor of 4.4 in the given simulation condition. The effect of the concentration of SO_2 on $[SO_4^{2-}]_T$ has been discussed in Sect. 4.1 above. Figure 5(e) shows the sensitivity of $[SO_4^{2-}]_T$ to the ATD loading (100, 200, and

400 μg m^{-3}). With the increasing of dust loading, the contribution of $[SO_4^{2-}]_{photo}$ to $[SO_4^{2-}]_T$ also increases. Figure 5(f) illustrates how sulfate formation is suppressed by different NO_x levels (also see Sect. 3.3.2).

The inorganic thermodynamic model (E–AIM II) was employed to estimate $[H^+]$ and the liquid water content ($M_{in,water}$) for the SO_4^{2-}–NH_4^+–H_2O system (excluding SO_4^{2-}(d_salt) in reaction 13 of Table 3: dust phase) (Eq. (8)) in both inorganic–salt seeded aqueous phase and dust phase chemistry. The uncertainty in $M_{in,water}$ and $[H^+]$ influences the partitioning tracers and consequently cause the uncertainty of $[SO_4^{2-}]_T$. The uncertainties in the prediction of $[H^+]$ using inorganic thermodynamic models are large because of the limited data (Clegg et al., 1998;Wexler and Clegg, 2002). In this study, $[H^+]$ is estimated by E–AIM II (Clegg et al., 1998;Wexler and Clegg, 2002;Clegg and Wexler, 2011) and corrected for the ammonia rich condition (Li et al., 2015;Li and Jang, 2012). The reported uncertainty of $[H^+]$ associated with the C–RUV method is ±18%. Figure S7 illustrates the uncertainties of the major model parameters ($[H^+]$, F_{water}, K_{d,SO_2}, k_{auto} and k_{OH,O_2}) and the prediction of $[SO_4^{2-}]_T$. The uncertainty of F_{water} ranges from -20% to 30% due to the uncertainty of the measurement of sulfate (±10%) and ammonia ions (±10%) using PILS-IC. The propagation error in Eqs. (6) and (7) is used to estimate the uncertainty of K_{d,SO_2} (-20% to 30%). The uncertainty of k_{auto} (-48% to 42%) and k_{OH,O_2} (-20% to 22%) are estimated by simulating $[SO_4^{2-}]_T$ within the uncertainty of K_{d,SO_2} and the measurement of sulfate (±10%). The uncertainty of $[SO_4^{2-}]_T$ was estimated to be ±12% at the end of the simulation. In this model, the Henry's law constant that is applied to gas–dust partitioning of tracers (Sect. 3.2.1) may lead to some biases in the prediction of sulfate and nitrate.

6 Conclusion and atmospheric implication

The AMAR model of this study was developed to predict the oxidation of SO_2 and NO_x using comprehensive kinetic mechanisms in the gas phase, inorganic seeded aqueous phase and dust phase. The thermodynamic parameters engaged in the partitioning process between gas, inorganic salted aqueous aerosol and dust phases were obtained from known data in the literature (Table 3), and the kinetic parameters for dust chemistry were estimated using previously reported indoor chamber data (Park and Jang, 2016). Overall, the AMAR simulations were consistent with experimentally observed outdoor chamber data (Fig. 3 and Fig. 4) under ambient sunlight. As

discussed in the sensitivity analysis (Sect. 5), both the $[SO_4^{2-}]_T$ and the relative distribution of mechanism–based sulfate formation are sensitive to all major variables (model inputs) including temperature, humidity, sunlight intensity, the quantity of dust loading, and concentrations of NO_x and SO_2.

In order to assess the importance of dust chemistry in ambient conditions, the prediction of sulfate formation in the presence of ATD dust needs to be extended to 24–hour simulations under various environmental conditions. Figure S8 shows the output simulated for 24 hours with 200 μg m^3 of ATD particle loading under urban (40 ppb NO_x; VOC/NO_x < 5; 20 ppb SO_2) and rural atmospheres (5 ppb NO_x; VOC/NO_x > 20; 2 ppb SO_2). At nighttime, when the temperature drops and humidity increases (70–90%, Fig. S6), the contribution of $[SO_4^{2-}]_{auto}$ to $[SO_4^{2-}]_T$ becomes larger than the typical chamber simulation during the daytime. In a rural environment, $[SO_4^{2-}]_{photo}$ is still the most influential on sulfate formation (0.76 fraction of $[SO_4^{2-}]_T$ in Fig. S8(a)). For the simulation in a polluted area (Fig. S8(b)), the fraction of $[SO_4^{2-}]_{photo}$ to $[SO_4^{2-}]_T$ significantly decreases (0.61) because of the suppression induced by NO_x (Sect. 3.3.2), but the fraction of $[SO_4^{2-}]_{auto}$ to $[SO_4^{2-}]_T$ increases (0.28). With decreasing sunlight intensity (after 5 PM), Fig. S8 shows the rapid increases in $[SO_4^{2-}]_{auto}$ due to the reaction of dust–phase SO_2 with ozone, which is the result of daytime photooxidation (Sect. 3.3.1). Fig. S8 suggests that the failure to predict sulfate formation without accurate dust chemistry ($[SO_4^{2-}]_{auto}$ + $[SO_4^{2-}]_{photo}$) can lead to substantial underestimation of the quantity of total sulfate at regional or global scales. SO_2 autoxidation alone may partially improve the prediction of sulfate in the presence of mineral dust, but sulfate production can still be largely underestimated and incorrectly predicted in time series when heterogeneous photocatalytic reactions in kinetic mechanisms are not considered.

The ATD particles in this study have chemical and physical properties different from ambient mineral dust particles. In general, the uptake coefficient of SO_2 in authentic mineral dust particles (e.g. Gobi Desert dust and Saharan dust) is known to be higher than that of ATD particles (Crowley et al., 2010). Thus, the effect of ambient dust particles on heterogeneous photocatalytic oxidation would be much more important than that of the ATD particles of this study. To extend the AMAR model derived with ATD particle to the prediction of sulfate in the presence of ambient dust particles, the model parameters related to rate constants and the physical characteristics (e.g. surface area and hygroscopic properties) of dust particles need to be modulated with laboratory experiments. The photoactivation rate constant ($k_{e\_h}^{j}$ in Sect. 3.2.3) to form electron-hole pairs

should be revisited to apply the model to different mineral dust systems, which are different from ATD in the photocatalytic capacity of conductive metal oxides. In addition to reactions of inorganic species, the influence of organic species (e.g., HCOOH, HCHO, and CH_3CHO) on dust heterogeneous chemistry needs to be investigated in the future.

5 Acknowledgments

This work was supported by grants from the National Institute of Metrological Science (NIMS–2016–3100), the Ministry of Science, ICT, and Future Planning at South Korea (2014M3C8A5032316) and the Fulbright Scholar (from USA to Mongolia).

Reference

Adams, J. W., Rodriguez, D., and Cox, R. A.: The uptake of SO2 on Saharan dust: a flow tube study, Atmos Chem Phys, 5, 2679-2689, 2005.

Atkinson, R., Baulch, D., Cox, R., Hampson Jr, R., Kerr, J., Rossi, M., and Troe, J.: Evaluated kinetic and photochemical data for atmospheric chemistry: supplement VI. IUPAC subcommittee on gas kinetic data evaluation for atmospheric chemistry, Journal of Physical and Chemical Reference Data, 26, 1329-1499, 1997.

Beardsley, R., Jang, M., Ori, B., Im, Y., Delcomyn, C. A., and Witherspoon, N.: Role of sea salt aerosols in the formation of aromatic secondary organic aerosol: yields and hygroscopic properties, Environ Chem, 10, 167-177, 10.1071/En13016, 2013.

Beardsley, R. L., and Jang, M.: Simulating the SOA formation of isoprene from partitioning and aerosol phase reactions in the presence of inorganics, Atmos Chem Phys, 16, 5993-6009, 2016.

Becker, K. H., Kleffmann, J., Kurtenbach, R., and Wiesen, P.: Solubility of nitrous acid (HONO) in sulfuric acid solutions, The Journal of Physical Chemistry, 100, 14984-14990, 1996.

Binkowski, F. S., and Roselle, S. J.: Models-3 Community Multiscale Air Quality (CMAQ) model aerosol component 1. Model description, Journal of geophysical research: Atmospheres, 108, 2003.

Bond, T. C.: Spectral dependence of visible light absorption by carbonaceous particles emitted from coal combustion, Geophys Res Lett, 28, 4075-4078, Doi 10.1029/2001gl013652, 2001.

Bongartz, A., Kames, J., Welter, F., and Schurath, U.: Near-UV absorption cross sections and trans/cis equilibrium of nitrous acid, The Journal of Physical Chemistry, 95, 1076-1082, 1991.

Byun, D., and Schere, K. L.: Review of the governing equations, computational algorithms, and other components of the models-3 Community Multiscale Air Quality (CMAQ) modeling system, Appl Mech Rev, 59, 51-77, 10.1115/1.2128636, 2006.

Chameides, W. L.: The photochemistry of a remote marine stratiform cloud, Journal of Geophysical Research: Atmospheres, 89, 4739-4755, 1984.

Chang, R. Y. W., Sullivan, R. C., and Abbatt, J. P. D.: Initial uptake of ozone on Saharan dust at atmospheric relative humidities, Geophys Res Lett, 32, Artn L14815 10.1029/2005gl023317, 2005.

Chen, H. H., Nanayakkara, C. E., and Grassian, V. H.: Titanium Dioxide Photocatalysis in Atmospheric Chemistry, Chem Rev, 112, 5919-5948, 10.1021/cr3002092, 2012.

Clegg, S., and Wexler, A. S.: Densities and Apparent Molar Volumes of Atmospherically Important Electrolyte Solutions. 2. The Systems $H^+ - HSO_4^- - SO_4^{2-} - H_2O$ from 0 to 3 mol kg^{-1} as a Function of Temperature and $H^+ - NH_4^+ - HSO_4^- - SO_4^{2-} - H_2O$ from 0 to 6 mol kg^{-1} at 25° C Using a Pitzer Ion Interaction Model, and $NH_4HSO_4 - H_2O$ and $(NH_4)_3H(SO_4)_2 - H2O$ over the Entire Concentration Range, The Journal of Physical Chemistry A, 115, 3461-3474, 2011.

Clegg, S. L., Brimblecombe, P., and Wexler, A. S.: Thermodynamic model of the system H^+-NH_4^+-SO_4^{2-}-NO_3^--H_2O at tropospheric temperatures, The Journal of Physical Chemistry A, 102, 2137-2154, 1998.

Colberg, C., Luo, B., Wernli, H., Koop, T., and Peter, T.: A novel model to predict the physical state of atmospheric $H_2SO_4/NH_3/H_2O$ aerosol particles, Atmos Chem Phys, 3, 909-924, 2003.

Colmenares, J. C., and Luque, R.: Heterogeneous photocatalytic nanomaterials: prospects and challenges in selective transformations of biomass-derived compounds, Chem Soc Rev, 43, 765-778, 10.1039/c3cs60262a, 2014.

Crowley, J. N., Ammann, M., Cox, R. A., Hynes, R. G., Jenkin, M. E., Mellouki, A., Rossi, M. J., Troe, J., and Wallington, T. J.: Evaluated kinetic and photochemical data for atmospheric chemistry: Volume V - heterogeneous reactions on solid substrates, Atmos Chem Phys, 10, 9059-9223, 10.5194/acp-10-9059-2010, 2010.

Cwiertny, D. M., Young, M. A., and Grassian, V. H.: Chemistry and photochemistry of mineral dust aerosol, Annu Rev Phys Chem, 59, 27-51, 10.1146/annurev.physchem.59.032607.093630, 2008.

Dong, X., Fu, J. S., Huang, K., Tong, D., and Zhuang, G.: Model development of dust emission and heterogeneous chemistry within the Community Multiscale Air Quality modeling system and its application over East Asia, Atmos. Chem. Phys., 16, 8157-8180, 10.5194/acp-16-8157-2016, 2016.

Dupart, Y., King, S. M., Nekat, B., Nowak, A., Wiedensohler, A., Herrmann, H., David, G., Thomas, B., Miffre, A., Rairoux, P., D'Anna, B., and George, C.: Mineral dust photochemistry induces nucleation events in the presence of SO_2, P Natl Acad Sci USA, 109, 20842-20847, 10.1073/pnas.1212297109, 2012.

Dupart, Y., Fine, L., D'Anna, B., and George, C.: Heterogeneous uptake of NO_2 on Arizona Test Dust under UV-A irradiation: An aerosol flow tube study, Aeolian Res, 15, 45-51, 10.1016/j.aeolia.2013.10.001, 2014.

Gankanda, A., Coddens, E. M., Zhang, Y., Cwiertny, D. M., and Grassian, V. H.: Sulfate formation catalyzed by coal fly ash, mineral dust and iron (iii) oxide: variable influence of temperature and light, Environmental Science: Processes & Impacts, 18, 1484-1491, 2016.

Goodman, A. L., Li, P., Usher, C. R., and Grassian, V. H.: Heterogeneous uptake of sulfur dioxide on aluminum and magnesium oxide particles, J Phys Chem A, 105, 6109-6120, 10.1021/jp004423z, 2001.

Gustafsson, R. J., Orlov, A., Badger, C. L., Griffiths, P. T., Cox, R. A., and Lambert, R. M.: A comprehensive evaluation of water uptake on atmospherically relevant mineral surfaces: DRIFT spectroscopy, thermogravimetric analysis and aerosol growth measurements, Atmos Chem Phys, 5, 3415-3421, 2005.

Hoffmann, M. R., Martin, S. T., Choi, W. Y., and Bahnemann, D. W.: Environmental Applications of Semiconductor Photocatalysis, Chem Rev, 95, 69-96, DOI 10.1021/cr00033a004, 1995.

Hoyle, C. R., Fuchs, C., Jarvinen, E., Saathoff, H., Dias, A., El Haddad, I., Gysel, M., Coburn, S. C., Trostl, J., Bernhammer, A. K., Bianchi, F., Breitenlechner, M., Corbin, J. C., Craven, J., Donahue, N. M., Duplissy, J., Ehrhart, S., Frege, C., Gordon, H., Hoppel, N., Heinritzi, M., Kristensen, T. B., Molteni, U., Nichman, L., Pinterich, T., Prevot, A. S. H., Simon, M., Slowik, J. G., Steiner, G., Tome, A., Vogel, A. L., Volkamer, R., Wagner, A. C., Wagner, R., Wexler, A. S., Williamson, C., Winkler, P. M., Yan, C., Amorim, A., Dommen, J., Curtius, J., Gallagher, M. W., Flagan, R. C., Hansel, A., Kirkby, J., Kulmala, M., Mohler, O., Stratmann, F., Worsnop, D. R., and Baltensperger, U.: Aqueous phase oxidation of sulphur dioxide by ozone in cloud droplets, Atmos Chem Phys, 16, 1693-1712, 10.5194/acp-16-1693-2016, 2016.

Huang, L. B., Zhao, Y., Li, H., and Chen, Z. M.: Kinetics of Heterogeneous Reaction of Sulfur Dioxide on Authentic Mineral Dust: Effects of Relative Humidity and Hydrogen Peroxide, Environ Sci Technol, 49, 10797-10805, 10.1021/acs.est.5b03930, 2015.

Jang, J., Jang, M., Mui, W., Delcomyn, C. A., Henley, M. V., and Hearn, J. D.: Formation of active chlorine oxidants in saline-oxone aerosol, Aerosol Sci Tech, 44, 1018-1026, 2010.

Krueger, B. J., Grassian, V. H., Laskin, A., and Cowin, J. P.: The transformation of solid atmospheric particles into liquid droplets through heterogeneous chemistry: Laboratory insights into the processing of calcium containing mineral dust aerosol in the troposphere, Geophys Res Lett, 30, Artn 1148 10.1029/2002gl016563, 2003.

Li, J., and Jang, M.: Aerosol acidity measurement using colorimetry coupled with a reflectance UV-visible spectrometer, Aerosol Sci Tech, 46, 833-842, 2012.

Li, J., Jang, M., and Beardsley, R. L.: Dialkylsulfate formation in sulfuric acid-seeded secondary organic aerosol produced using an outdoor chamber under natural sunlight, Environ Chem, 2015.

Li, J. W., and Han, Z. W.: A modeling study of the impact of heterogeneous reactions on mineral aerosol surfaces on tropospheric chemistry over East Asia, Particuology, 8, 433-441, 10.1016/j.partic.2010.03.018, 2010.

Liang, J. Y., and Jacobson, M. Z.: A study of sulfur dioxide oxidation pathways over a range of liquid water contents, pH values, and temperatures, J Geophys Res-Atmos, 104, 13749-13769, Doi 10.1029/1999jd900097, 1999.

Linsebigler, A. L., Lu, G. Q., and Yates, J. T.: Photocatalysis on Tio2 Surfaces - Principles, Mechanisms, and Selected Results, Chem Rev, 95, 735-758, DOI 10.1021/cr00035a013, 1995.

Liu, C., Ma, Q. X., Liu, Y. C., Ma, J. Z., and He, H.: Synergistic reaction between SO_2 and NO_2 on mineral oxides: a potential formation pathway of sulfate aerosol, Phys Chem Chem Phys, 14, 1668-1676, 10.1039/c1cp22217a, 2012.

Liu, Y., Zhu, T., Zhao, D., and Zhang, Z.: Investigation of the hygroscopic properties of $Ca(NO_3)_2$ and internally mixed Ca $(NO_3)_2/CaCO_3$ particles by micro-Raman spectrometry, Atmos Chem Phys, 8, 7205-7215, 2008.

Ma, Q. X., Liu, Y. C., and He, H.: Synergistic effect between NO_2 and SO_2 in their adsorption and reaction on gamma-alumina, J Phys Chem A, 112, 6630-6635, 10.1021/jp802025z, 2008.

Martell, A. E., and Smith, R. M.: Inorganic complexes, Plenum Press, 1976.

McNaught, A. D., and Wilkinson, A.: IUPAC. Compendium of Chemical Terminology, 2nd ed. (the "Gold Book"), WileyBlackwell; 2nd Revised edition edition, 1997.

Michel, A. E., Usher, C. R., and Grassian, V. H.: Reactive uptake of ozone on mineral oxides and mineral dusts, Atmos Environ, 37, 3201-3211, 10.1016/S1352-2310(03)00319-4, 2003.

Nanayakkara, C. E., Pettibone, J., and Grassian, V. H.: Sulfur dioxide adsorption and photooxidation on isotopically-labeled titanium dioxide nanoparticle surfaces: roles of surface hydroxyl groups and adsorbed water in the formation and stability of adsorbed sulfite and sulfate, Phys Chem Chem Phys, 14, 6957-6966, 10.1039/c2cp23684b, 2012.

Navea, J. G., Chen, H. H., Huang, M., Carmichel, G. R., and Grassian, V. H.: A comparative evaluation of water uptake on several mineral dust sources, Environ Chem, 7, 162-170, 10.1071/En09122, 2010.

Park, J., and Jang, M.: Heterogeneous photooxidation of sulfur dioxide in the presence of airborne mineral dust particles, RSC Advances, 6, 58617-58627, 2016.
Reyes-Coronado, D., Rodríguez-Gattorno, G., Espinosa-Pesqueira, M., Cab, C., De Coss, R., and Oskam, G.: Phase-pure TiO_2 nanoparticles: anatase, brookite and rutile, Nanotechnology, 19, 145605, 2008.
Saliba, N., Moussa, S., and El Tayyar, G.: Contribution of airborne dust particles to HONO sources, Atmospheric Chemistry and Physics Discussions, 14, 4827-4839, 2014.
Saliba, N. A., and Chamseddine, A.: Uptake of acid pollutants by mineral dust and their effect on aerosol solubility, Atmos Environ, 46, 256-263, 10.1016/j.atmosenv.2011.09.074, 2012.
Sarwar, G., Fahey, K., Kwok, R., Gilliam, R. C., Roselle, S. J., Mathur, R., Xue, J., Yu, J., and Carter, W. P.: Potential impacts of two SO_2 oxidation pathways on regional sulfate concentrations: aqueous-phase oxidation by NO_2 and gas-phase oxidation by Stabilized Criegee Intermediates, Atmos Environ, 68, 186-197, 2013.
Sarwar, G., Simon, H., Fahey, K., Mathur, R., Goliff, W. S., and Stockwell, W. R.: Impact of sulfur dioxide oxidation by Stabilized Criegee Intermediate on sulfate, Atmos Environ, 85, 204-214, 2014.
Schwartz, S., and White, W.: Solubility equilibria of the nitrogen oxides and oxyacids in dilute aqueous solution, Adv. Environ. Sci. Eng.;(United States), 4, 1981.
Schwartz, S. E.: Gas-Phase and Aqueous-Phase Chemistry of HO_2 in Liquid Water Clouds, J Geophys Res-Atmos, 89, 1589-1598, DOI 10.1029/JD089iD07p11589, 1984.
Shang, J., Li, J., and Zhu, T.: Heterogeneous reaction of SO_2 on TiO_2 particles, Sci China Chem, 53, 2637-2643, 10.1007/s11426-010-4160-3, 2010.
Tang, M. J., Cziczo, D. J., and Grassian, V. H.: Interactions of Water with Mineral Dust Aerosol: Water Adsorption, Hygroscopicity, Cloud Condensation, and Ice Nucleation, Chem Rev, 116, 4205-4259, 10.1021/acs.chemrev.5b00529, 2016.
Tang, Y. H., Carmichael, G. R., Kurata, G., Uno, I., Weber, R. J., Song, C. H., Guttikunda, S. K., Woo, J. H., Streets, D. G., Wei, C., Clarke, A. D., Huebert, B., and Anderson, T. L.: Impacts of dust on regional tropospheric chemistry during the ACE-Asia experiment: A model study with observations, J Geophys Res-Atmos, 109, Artn D19s21 10.1029/2003jd003806, 2004.
Thiebaud, J., Thevenet, F., and Fittschen, C.: OH Radicals and H2O2 Molecules in the Gas Phase near to TiO2 Surfaces, J Phys Chem C, 114, 3082-3088, 10.1021/jp9102542, 2010.
Thompson, T. L., and Yates, J. T.: Surface science studies of the photoactivation of TiO_2 new photochemical processes, Chem Rev, 106, 4428-4453, 2006.
Ullerstam, M., Vogt, R., Langer, S., and Ljungstrom, E.: The kinetics and mechanism of SO_2 oxidation by O_3 on mineral dust, Phys Chem Chem Phys, 4, 4694-4699, 10.1039/b203529b, 2002.
Underwood, G. M., Song, C. H., Phadnis, M., Carmichael, G. R., and Grassian, V. H.: Heterogeneous reactions of NO_2 and HNO_3 on oxides and mineral dust: A combined laboratory and modeling study, J Geophys Res-Atmos, 106, 18055-18066, Doi 10.1029/2000jd900552, 2001.
Usher, C. R., Al-Hosney, H., Carlos-Cuellar, S., and Grassian, V. H.: A laboratory study of the heterogeneous uptake and oxidation of sulfur dioxide on mineral dust particles, J Geophys Res-Atmos, 107, Artn 4713 10.1029/2002jd002051, 2002.

Usher, C. R., Michel, A. E., Stec, D., and Grassian, V. H.: Laboratory studies of ozone uptake on processed mineral dust, Atmos Environ, 37, 5337-5347, 10.1016/j.atmosenv.2003.09.014, 2003.

Vlasenko, A., Sjogren, S., Weingartner, E., Stemmler, K., Gaggeler, H. W., and Ammann, M.: Effect of humidity on nitric acid uptake to mineral dust aerosol particles, Atmos Chem Phys, 6, 2147-2160, 2006.

Wagner, C., Schuster, G., and Crowley, J.: An aerosol flow tube study of the interaction of N_2O_5 with calcite, Arizona dust and quartz, Atmos Environ, 43, 5001-5008, 2009.

Wagner, R., Ajtai, T., Kandler, K., Lieke, K., Linke, C., Muller, T., Schnaiter, M., and Vragel, M.: Complex refractive indices of Saharan dust samples at visible and near UV wavelengths: a laboratory study, Atmos Chem Phys, 12, 2491-2512, 10.5194/acp-12-2491-2012, 2012.

Wexler, A. S., and Clegg, S. L.: Atmospheric aerosol models for systems including the ions H^+, NH_4^+, Na^+, SO_4^{2-}, NO_3^-, Cl^-, Br^-, and H_2O, Journal of Geophysical Research: Atmospheres, 107, 2002.

Zhang, X. Y., Zhuang, G. S., Chen, J. M., Wang, Y., Wang, X., An, Z. S., and Zhang, P.: Heterogeneous reactions of sulfur dioxide on typical mineral particles, J Phys Chem B, 110, 12588-12596, 10.1021/jp0617773, 2006.

Zhang, Y.-H., and Chan, C. K.: Understanding the hygroscopic properties of supersaturated droplets of metal and ammonium sulfate solutions using Raman spectroscopy, The Journal of Physical Chemistry A, 106, 285-292, 2002.

Zhong, M., and Jang, M.: Light absorption coefficient measurement of SOA using a UV-Visible spectrometer connected with an integrating sphere, Atmos Environ, 45, 4263-4271, 10.1016/j.atmosenv.2011.04.082, 2011.

Zuend, A., Marcolli, C., Booth, A., Lienhard, D., Soonsin, V., Krieger, U., Topping, D., McFiggans, G., Peter, T., and Seinfeld, J.: New and extended parameterization of the thermodynamic model AIOMFAC: calculation of activity coefficients for organic-inorganic mixtures containing carboxyl, hydroxyl, carbonyl, ether, ester, alkenyl, alkyl, and aromatic functional groups, Atmos Chem Phys, 11, 9155-9206, 2011.

Table 1. Experiment conditions and simulation results for SO_2 heterogeneous photooxidation on the surface of ATD particles at variety condition of humidity (RH), light sources and initial concentration of traces using indoor chamber data.

Exp. No.[a]	UV	RH[b] (%)	Temp.[b] (K)	Initial Concentration				Duration[e] (min)	Exp.	Note[g]
				ATD dust[c] (μg m^{-3})	SO_2[d] (ppb)	NO/NO_2[d] (ppb)	O_3[d] (ppb)		$[SO_4^{2-}]_T$[f] (μg m^{-3})	
D1	Off	21.0	295.9	295	267	N.A.	N.A.	150	0.61±0.02	K_{d,SO_2},
D2	Off	55.3	295.0	406	152	0.1/0.6	1.86	148	1.02±0.01	k_{auto}
D3	Off	80.1	294.5	278	147	0.9/1.6	0.29	147	1.59±0.02	
L1	On	20.4	297.0	123	87.8	0.3/1.7	0.30	120	1.66±0.04	k_{OH,O_2},
L2	On	55.2	299.3	120	82.3	0.2/1.9	1.79	120	2.54±0.21	k_{auto}
L3	On	80.7	298.7	131	78.0	0.2/0.4	0.28	120	5.22±0.19	
L4	On	21.0	296.9	130	78.1	0.1/1.35	64.8	120	4.48±0.14	k_{OH,O_3},
D4	Off	20.4	296.6	293	101.0	0.7/1.9	65.4	60	0.158±0.01	k_{auto,O_3}

[a] "D" denotes experiments under dark condition. "L" denotes experiments with UV light. The dataset D1–D3 and L1–L4 were obtained from the recent laboratory data reported by Park and Jang (2016). Dataset D4 was newly added here to estimate the kinetic parameter of heterogeneous autoxidation of SO_2 in the presence of ozone.

[b] The accuracy of RH is ±5%. The accuracy of temperature is ±0.5 K.

[c] The mass concentration of ATD particles were calculated combining SMPS data, OPC data, the density of dust particles (2.65 g cm^{-3}), and the particle size distribution (<3μm). The errors associated with the dust particle mass concentration were ±6%.

[d] The errors associated with the observation of SO_2, NO, NO_2, and O_3 were ±0.9%, ±12.5%, ±6.9%, and ±0.2%, respectively.

[e] The duration is the simulation time from the beginning of the experiment to the end of the experiment.

[f] Sulfate concentrations were measured at the end of experiments using PILS–IC. The measurements were not corrected for the particle loss rate to the wall but corrected for the indigenous sulfate from dust particles.

[g] The experiments are noted with the associated kinetic parameters that were empirically determined.

Table 2. Outdoor chamber experiment condition for SO_2 heterogeneously photooxidation on the ATD particles at variety initial concentration of SO_2, dust particle, and NO_2.

Exp. Date	Purpose	RH[a] (%)	Temp.[a] (K)	simulation Time (EST)	Initial Concentration[b]			
					ATD dust [c] ($\mu g\ m^{-3}$)	SO_2 (ppb)	NO/NO_2 (ppb)	O_3 (ppb)
28/3/2015	SO_2	18–67	277.1–301.9	11:10–16:30	N.A.	60.1	0.1/0.9	6.3
	SO_2 & dust	24–71	277.8–301.5	10:50–16:30	290.1	56.4	0.1/0.7	0.7
16/6/2015	Low dust	15–49	286.7–313.0	8:40–15:30	90.1	100.0	0.1/0.7	0.7
	High dust	16–48	287.0–311.5	9:30–15:30	403.7	120.1	1.1/1.0	5
12/11/2015	Low SO_2	24–71	277.8–301.5	8:40–17:30	239.2	119.0	0.5/2.0	3.0
	High SO_2	14–42	296.2–325.0	9:00–17:30	229.0	271.6	0.2/2.1	2.6
14/4/2017	NO_x effect	33–95	287.8–314.3	6:30–17:30	496.2	88.1	88.9/13.5	3.0
25/4/2017–1	NO_x effect	18–89	283.8–313.6	6:00–16:00	414.0	15.0	112.0/13.2	2.2
25/4/2017–2	NO_x effect	26–94	284.1–312.7	6:00–16:00	478.7	17.5	35.9/3.6	1.9

[a] The accuracy of RH is ±5%. The accuracy of temperature is ±0.5 K.

[b] The errors associated with the observation of SO_2, NO, NO_2, O_3, NH_4^+ and the concentration of dust particle mass were ±0.9%, ±12.5%, ±6.9%, ±0.2%, 5.0±% and ±6%, respectively. The detailed observations of the chemical species during the experiments were shown in Fig. S4 and Fig. S5 in Supporting Information.

[c] The mass concentration of ATD particles were calculated combining SMPS data, OPC data, the density of dust particles (2.65 g cm^{-3}), and the particle size distribution (<3μm) .

Table 3. Dust–phase heterogeneous reactions and their rate constants in the presence of ATD particles.

	Reaction [a]	Rate constant [b]	Coefficients of rate constants [b]		K_a [c]	Reference [d]	Note[e]
			k_1	k_2			
	Partitioning						
1	$SO_2 + Dust \rightarrow SO_2(d) + Dust$	k_{abs}	1×10^{-8}			AR05, HZ15	R7
2	$SO_2(d) \rightarrow SO_2$	k_{des}	1×10^{9}	3100	0.013	AR05, HZ15	R8
3	$O_3 + Dust \rightarrow O_3(d) + Dust$	k_{abs}	1×10^{-8}			MU03, US01	
4	$O_3(d) \rightarrow O_3$	k_{des}	3×10^{10}	2700	0	MU03, US01	
5	$NO_2 + Dust \rightarrow NO_2(d) + Dust$	k_{abs}	1×10^{-8}			CW84	
6	$NO_2(d) \rightarrow NO_2$	k_{des}	1×10^{10}	2500	0	CW84	
7	$HNO_3 + Dust \rightarrow HNO_3(d) + Dust$	k_{abs}	1×10^{-8}			SW81, Sc84	
8	$HNO_3(d) \rightarrow HNO_3$	k_{des}	1×10^{15}	8700	15.4	SW81, Sc84	
9	$HONO + Dust \rightarrow HONO(d) + Dust$	k_{abs}	1×10^{-8}			BK96	
10	$HONO(d) \rightarrow HONO$	k_{des}	1×10^{10}	4900	0	BK96	
11	$N_2O_5 + Dust \rightarrow HNO_3(d) + Dust$	k_{abs}	7.3×10^{-3}			WS09	
	Dust phase						
1	$Dust + h\upsilon \rightarrow Dust + e\_h$	$k^j_{e\_h}$	$j_{[ATD]}$			Sect. 3.2.3	R10
2	$e\_h \rightarrow energy$	k_{recom}	1×10^{-2}			Sect. 3.2.3	R11
3	$e\_h + O_2 \rightarrow OH(d)$	k_{OH,O_2}	1×10^{-22}	2.3RH		Sect. 3.2.3	R12
4	$SO_2(d) \rightarrow SO_4^{2-}(d)$	k_{auto}	5×10^{-6}			Sect. 3.2.2	R9
5	$SO_2(d) + OH(d) \rightarrow SO_4^{2-}(d)$	k_{photo}	1×10^{-12}			Sect. 3.2.4	R13
6	$SO_2(d) + O_3(d) \rightarrow SO_4^{2-}(d) + O_2$	k_{auto,O_3}	2×10^{-11}			Sect. 3.3.1	R14
7	$e\_h + O_3(d) \rightarrow OH(d) + O_2$	k_{OH,O_3}	1×10^{-12}			Sect. 3.3.1	R15
8	$NO_2(d) \rightarrow NO_3^-(d)$	k_{auto,NO_2}	6×10^{-5}			Sect. 3.3.2	R18
9	$e\_h + NO_2(d) \rightarrow HONO(d)$	k_{e_h,NO_2}	6×10^{-12}			Sect. 3.3.2	R16
10	$HONO(d) + h\upsilon \rightarrow OH(d) + NO$	k^j_{HONO}	$j_{[HONO\_to\_OH]}$			BK91, AB97	R17
11	$NO_2(d) + OH(d) \rightarrow NO_3^-(d)$	k_{photo,NO_2}	1×10^{-10}			Sect. 3.3.2	R19

[a] The unit of the chemical species (except dust) is molecule cm^{-3} for both partitioning process and the dust phase chemistry. The unit of the dust for model input is mass concentration ($\mu g\ m^{-3}$) and is multiplied by a factor of 2.45×10^{10} for simulation.

[b] The unit of reaction rate constants is s^{-1} for the first order reactions and cm^3 molecule^{-1} s^{-1} for the second order reactions.

k_{abs} is uptake rate constant. $k_{abs} = k_1\ \omega\ f_{dust,Mass\_to\_Surface}$ / 4, where $\omega = \sqrt{8\ R\ T/(\pi\ MW)}$ (m s^{-1}) and $f_{dust,Mass\_to\_Surface}$ = 3.066×10^{-6} (m^2 μg). R is the ideal gas constant and MW (g mol^{-1}) is the molecule weight of chemical species.

k_{des} is desorption rate constant. $k_{des} = k_1 \exp\left(-\frac{k_2}{T}\right)/(F_{water}(1 + K_a/[H^+]))$, where F_{water} is calculated using Eq. (8). $[H^+]$ is dynamically calculated based on thermodynamic model (E–AIM II) (Clegg et al., 1998;Wexler and Clegg, 2002;Clegg and Wexler, 2011).

The rate constants (k) for dust phase reactions is $k=k_1\exp(k_2)$.

$k^j_{e\_h}$ and k^j_{HONO} are photocatalytic reaction rates. The cross sections and quantum yields of dust are estimated (see Sect. 2.2).

[c] Coefficient K_a is acid dissociation constant (see k_{des}).

[d] The rate constant parameters, which are noted as "this study", are determined using the simulation of indoor chamber data(Park and Jang, 2016) (see Sect. 3). AB97, Atkinson et al. (1997); AR05, Adams et al. (2005); BK91, Bongartz et al. (1991); BK96, Becker et al. (1996); CW84, Chameides (1984); HZ15, Huang et al. (2015); MU03, Michel et al. (2003); Sc84, Schwartz (1984); SW81, Schwartz and White (1981); US01, Underwood et al. (2001); WS09, Wagner et al. (2009).

[e] The reactions are noted with the numbers associated with the reaction in main text.

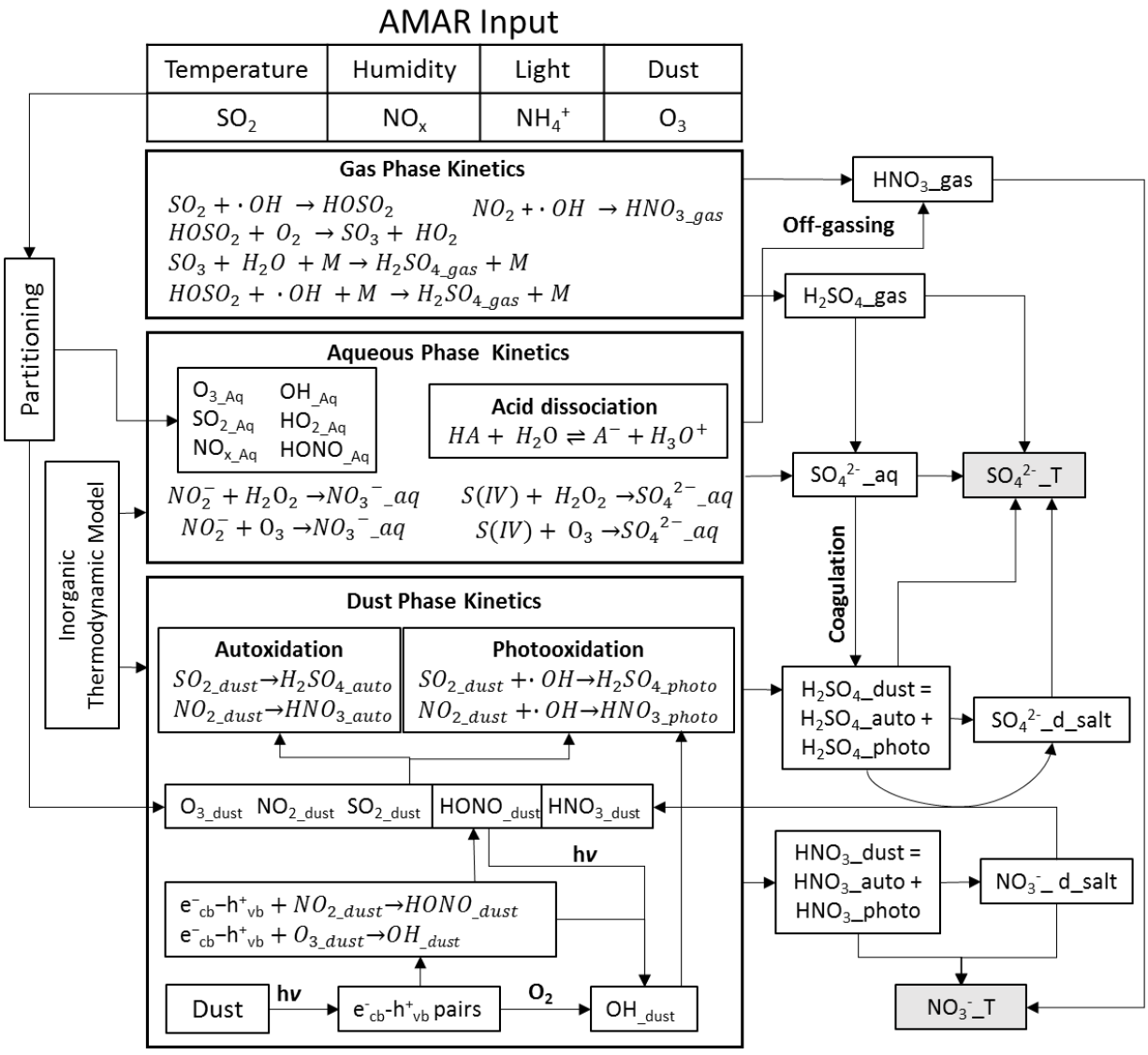

Figure 1. The overall schematic of the AMAR model to simulate heterogeneous SO_2 oxidation. For the description of chemical species, gas phase, aqueous phase and dust phase are symbolized as "gas", "aq" and "dust", respectively. SO_4^{2-}_T, H_2SO_4_gas, SO_4^{2-}_aq and H_2SO_4_dust are the total sulfate formation and the formation of sulfate from gas phase, aqueous phase and dust phase, respectively. SO_4^{2-}_d_salt and NO_3^-_d_salt are the neutralized sulfate and nitrate in dust phase.

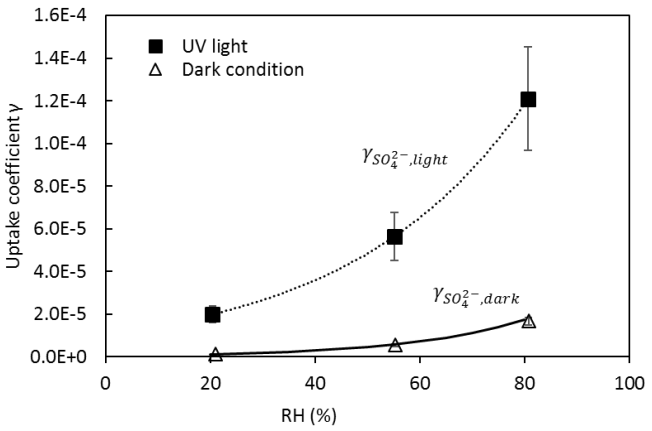

Figure 2. Uptake coefficient (γ) of SO_2 in the presence of the ATD particles under dark condition and UV light condition. The values of γ were obtained by kinetic model using indoor experimental data. The $\gamma_{SO_4^{2-},light}$ is correlated to concentration of OH radicals and RH (%). The $\gamma_{SO_4^{2-},dark}$ is a function of RH. The error bar of γ was derived from the model uncertainty.

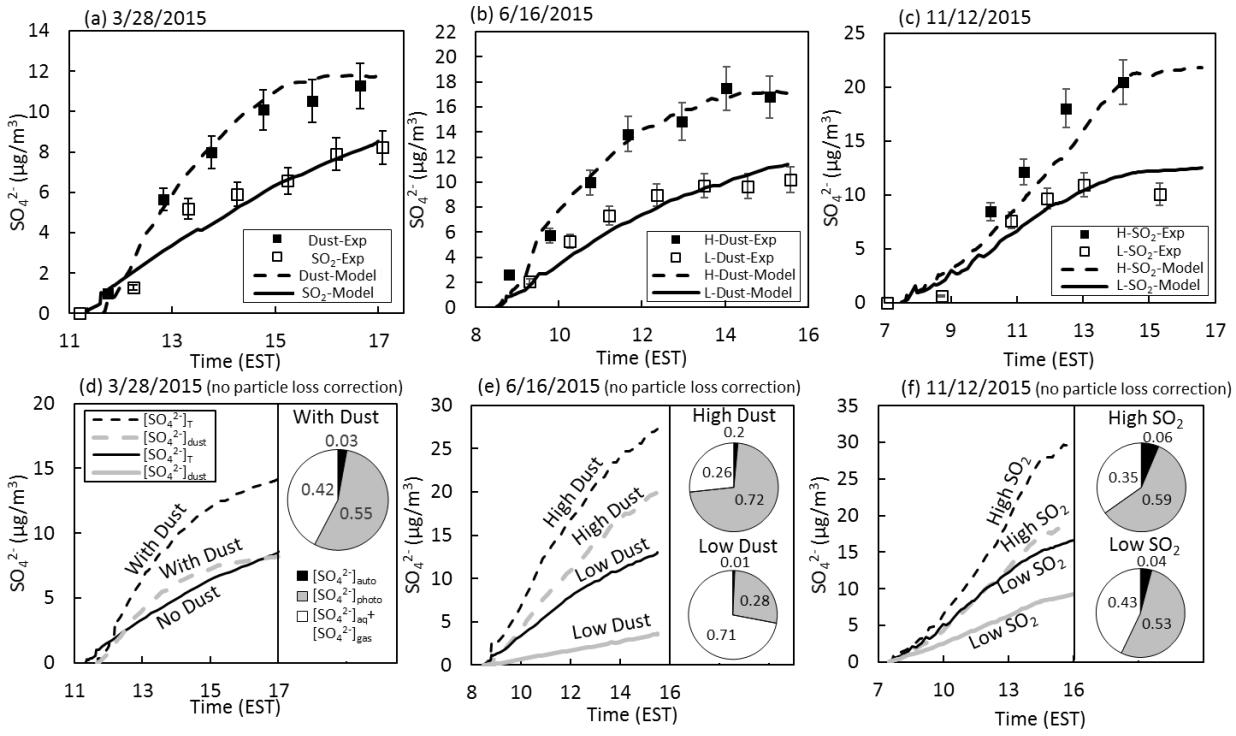

Figure 3. Time profiles of total sulfate concentration (SO_4^{2-}, μg m^{-3}) in the UF–APHOR. "Exp" denotes the experimentally observed sulfate ($[SO_4^{2-}]_T$) and "Model" denotes the model–predicted sulfate. "H" and "L" represent the high and the low initial concentrations of chemical species. The errors associated with the concentration of sulfate is ±10% originated form the PILS–IC measurement. (a) Sulfate formation with and without ATD particles (SO_2 60 ppb vs. SO_2 56 ppb and dust 290 μg m^{-3}). (b) The high and low loadings of dust particles (dust 90 μg m^{-3} and SO_2 100 ppb vs. dust 404 μg m^{-3} and SO_2 120 ppb). (c) The high and the low concentrations of SO_2 (SO_2 119 ppb and dust 239 μg m^{-3} vs. SO_2 272 ppb and dust 230 μg m^{-3}). For Fig. 3(a), 3(b) and 3(c), the simulations included the chamber dilution and the wall process of gaseous compounds and particles (Sect. S1). For Fig. 3(d), 3(e) and 3(f), the wall process for the particle loss was excluded to estimate the influence of ATD particles on sulfate formation without the chamber artefacts. In Fig. 3(d), 3(e) and 3(f), total sulfate was decoupled into the sulfate originated from dust chemistry ($[SO_4^{2-}]_{dust}=[SO_4^{2-}]_{photo}+[SO_4^{2-}]_{auto}$). The pie charts inserted into Fig. 3(d), 3(e) and 3(f) illustrate how total sulfate is attributed to major pathways at the end of the experiments.

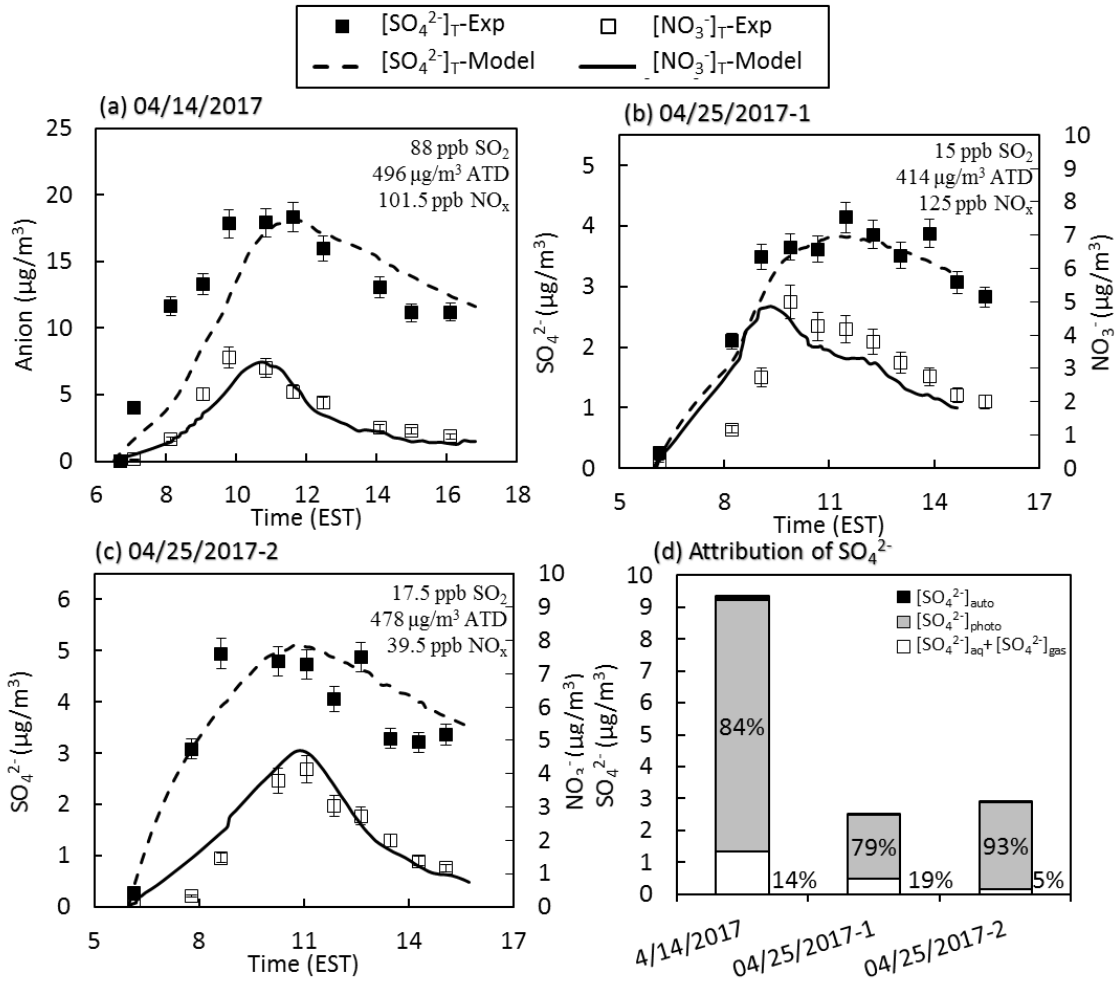

Figure 4. Time profiles of total sulfate concentration ($[SO_4^{2-}]_T$, μg/m^3) and nitrate concentration ($[NO_3^-]_T$, μg m^{-3}) in the dual chamber experiments using UF–APHOR at different NO_x levels. The concentrations of sulfate and nitrate were measured using PILS–IC during the experiments. The error bars of the concentration of sulfate and nitrate is ±10% originated form the PILS–IC measurement. The detailed experimental conditions of Fig. 4(a), Fig. 4(b), and Fig. 4(c) are shown in Table 2. Figure 4(d) shows how total sulfate is attributed to aqueous phase reaction (sulfate formation in gas phase + sulfate formation in inorganic salted inorganic aqueous phase) ($[SO_4^{2-}]_{aq}$+$[SO_4^{2-}]_{gas}$), dust–phase autoxidation ($[SO_4^{2-}]_{auto}$), and dust photochemistry ($[SO_4^{2-}]_{photo}$) at the end of the experiments. "Exp" denotes the experimental observation and "Model" denotes the simulation using the AMAR module. The chamber dilution and the wall process of gaseous compounds and particles were included in the simulation (Sect. S1).

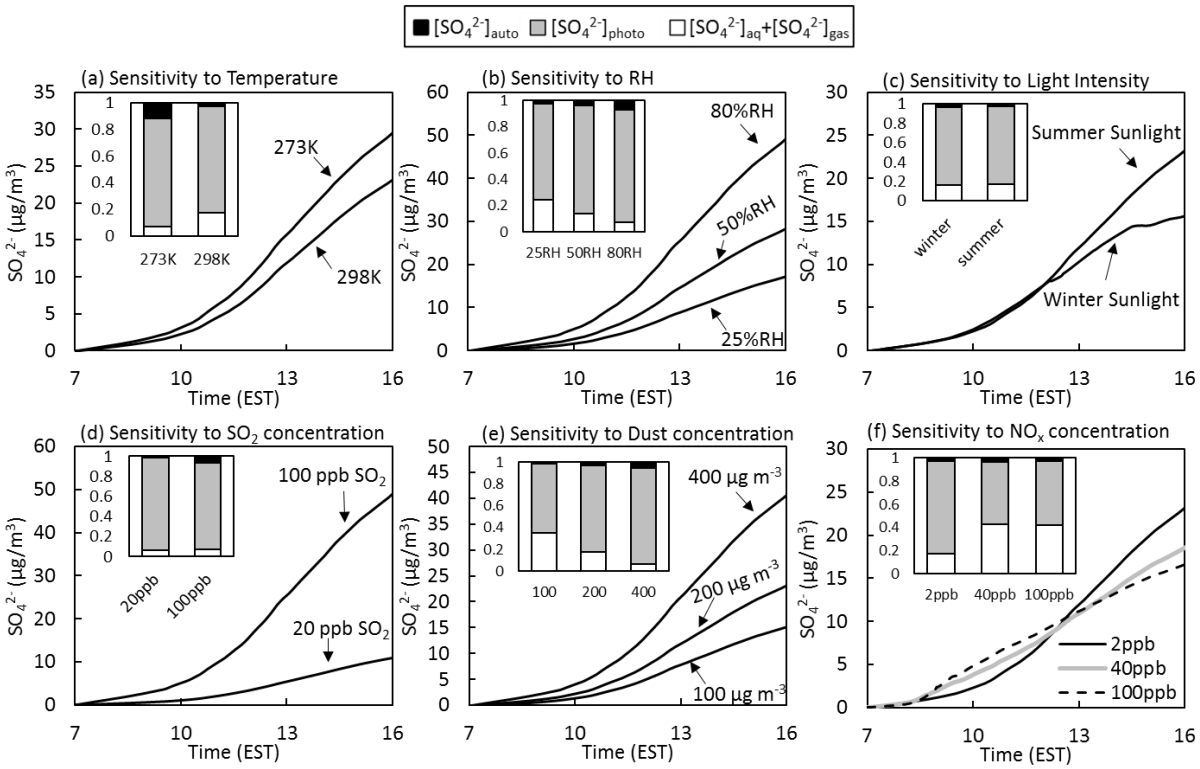

Figure 5. Sensitivity test of AMAR model to (a) temperature at 273K and 298K; (b) RH at 25%, 50% and 80%; (c) sunlight profiles of summertime (25 April, 2017) and wintertime (12 November, 2015) at Gainesville, Florida (latitude/longitude: 29.64185°/–82.347883°); (d) the concentration of SO_2; (e) the concentration of dust particles; and (f) the NO_x concentration (initial $NO:NO_2$=1:1). The stacked column chart in each figure illustrates how total sulfate is attributed to major pathways at the end of each experiment. For the sensitivity test, the chamber simulation is conducted with 100 ppb of initial SO_2, 2 ppb of initial NO_2, 2 ppb of initial O_3 and 200 μg m^{-3} of ATD particles at T = 298K and RH = 40% under ambient sunlight on 25 April 2017. NO_x (rate of flux = 2.7×10^6, s^{-1}) and isoprene (rate of flux = 2.7×10^6, s^{-1}) were constantly added to simulate chamber dilution. The simulation was performed without considering the particle loss to the chamber wall.